Nucleic Acids Research, 2023, **51**, 12224–12241
https://doi.org/10.1093/nar/gkad952
Advance access publication date: 11 November 2023
Genome integrity, repair and replication

TATDN2 resolution of R-loops is required for survival of BRCA1-mutant cancer cells

Aruna S. Jaiswal[1], Arijit Dutta[2], Gayathri Srinivasan[1], Yaxia Yuan[2], Daohong Zhou[2], Montaser Shaheen[1], Doraid T. Sadideen[1], Austin Kirby[1], Elizabeth A. Williamson[1], Yogesh K. Gupta[2], Shaun K. Olsen[2], Mingjiang Xu[3], Eva Loranc[4], Pramiti Mukhopadhyay[4], Alexander Pertsemlidis[4], Alexander J.R. Bishop[4], Patrick Sung[2], Jac A. Nickoloff[5,*] and Robert Hromas[1,*]

[1]Department of Medicine and the Mays Cancer Center, the University of Texas Health Science Center San Antonio, San Antonio, TX 78229, USA
[2]Department of Biochemistry and Structural Biology and the Greehey Children's Cancer Research Institute, the University of Texas Health Science Center San Antonio, San Antonio, TX 78229, USA
[3]Department of Molecular Medicine and the Mays Cancer Center, the University of Texas Health Science Center San Antonio, San Antonio, TX 78229, USA
[4]Department of Cell Systems and Anatomy and the Greehey Children's Cancer Research Institute, the University of Texas Health Science Center San Antonio, San Antonio, TX 78229, USA
[5]Department of Environmental and Radiological Health Sciences, College of Veterinary Medicine and Biomedical Sciences, Colorado State University, Fort Collins, CO 80523, USA

*To whom correspondence should be addressed. Tel: +1 210 567 4432; Email: hromas@uthscsa.edu
Correspondence may also be addressed to Jac A. Nickoloff. Tel: +1 970 491 6674; Email: J.Nickoloff@colostate.edu

Abstract

BRCA1-deficient cells have increased IRE1 RNase, which degrades multiple microRNAs. Reconstituting expression of one of these, miR-4638–5p, resulted in synthetic lethality in BRCA1-deficient cancer cells. We found that miR-4638-5p represses expression of TATDN2, a poorly characterized member of the TATD nuclease family. We discovered that human TATDN2 has RNA 3′ exonuclease and endonuclease activity on double-stranded hairpin RNA structures. Given the cleavage of hairpin RNA by TATDN2, and that BRCA1-deficient cells have difficulty resolving R-loops, we tested whether TATDN2 could resolve R-loops. Using *in vitro* biochemical reconstitution assays, we found TATDN2 bound to R-loops and degraded the RNA strand but not DNA of multiple forms of R-loops *in vitro* in a Mg^{2+}-dependent manner. Mutations in amino acids E593 and E705 predicted by Alphafold-2 to chelate an essential Mg^{2+} cation completely abrogated this R-loop resolution activity. Depleting TATDN2 increased cellular R-loops, DNA damage and chromosomal instability. Loss of TATDN2 resulted in poor replication fork progression in the presence of increased R-loops. Significantly, we found that TATDN2 is essential for survival of BRCA1-deficient cancer cells, but much less so for cognate BRCA1-repleted cancer cells. Thus, we propose that TATDN2 is a novel target for therapy of BRCA1-deficient cancers.

Graphical abstract

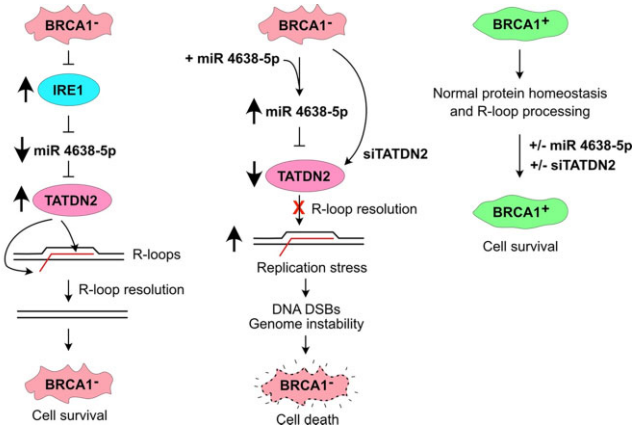

Received: May 28, 2023. **Revised:** October 3, 2023. **Editorial Decision:** October 8, 2023. **Accepted:** October 18, 2023

Introduction

The TATD nuclease family is highly conserved from bacteria to humans. There is one member in bacteria, TatD and three in humans, TATDN1 is most homologous to TatD, and TATDN2 and TATDN3 (1–4). Human TATDN2 is unique in that it has a large, disordered amino-terminal region that the other members lack, and it has differences in the nuclease domain (4–6). Bacterial TatD and human TATDN1 and 3 tertiary structures has been resolved by X-ray crystallography (4) and supports their Alphafold-2 predicted nuclease domain (1–7). Biochemical characterization of bacterial TatD found that it is a Mg^{2+}-dependent 3′ exonuclease preferring single-stranded (SS) RNA and DNA (2). Yeast and trypanosome TatD were found to mediate some of the genomic DNA cleavage seen after apoptosis (8,9). Bacterial and malarial TatD contribute to the virulence of infections with these organisms (10,11). Zebrafish TATDN1 cleaved supercoiled plasmid and kinetoplast catenated DNA to relaxed open circle and linear DNA (12). Depletion of TATDN1 in embryonic zebrafish leads to delays in cell cycle progression and abnormal chromosomal segregation (12). However, there has been less work on the function of the three human members of the family than in lower organisms. Integrating the diverse activities of TatD in lower organisms into a unified functional hypothesis for the entire family in higher organisms has not yet been accomplished.

R-loops form when RNA binds to a complementary DNA strand, displacing the opposing DNA strand, creating a stable double-stranded (DS) DNA bubble with an intercalated complementary RNA strand. This common triple-stranded structure occurs most often during transcription (13–15). R-loops have generated intense interest recently due to their contribution to chromosomal instability and resultant oncogenesis (15–17). R-loops are conserved from single cell organisms through humans and have multiple functions in normal nucleic acid metabolism. For example, R-loops can serve as a primer for initiating mitochondrial DNA replication (18,19). R-loops also promote class switch recombination of immunoglobulin heavy chains during B-cell maturation (20,21). Additionally, an alternative form of homology-directed DNA double-strand break (DSB) repair uses an RNA strand to bridge the DSB, forming an R-loop structure (22). In this context, these R-loop structures form adjacent to locally transcribed regions, and they recruit RAD52 to initiate homology-directed repair (23).

R-loops also play key roles in chromatin remodeling and subsequent gene expression (24,25). R-loops are enriched at gene promoters and 3′ transcription termination sites, and are associated with splicing, enhancers and super enhancers at topologically associating domain boundaries (14–17,24–28). R-loops may regulate epigenetic histone modifications (27,28), but since nucleosomes cannot form around R-loops, such chromatin regulation would be indirect, via recruitment of other mediators (15,29,30). Perhaps the most important and well characterized normal function of R-loops is the relaxation of topological stress caused by replication or transcription (31–33). Several studies have shown that negative supercoiling from DNA unwinding promotes R-loop formation which decreases the tense, high energy state of supercoiled DNA (34–37). Consistent with this, TOP1 and 2 deficiencies promote R-loop formation and topoisomerases are important in resolving R-loops (34–37).

However, it has been increasingly recognized that R-loops can have multiple pathological consequences as well. R-loops can lead to DSBs and chromosomal instability via multiple mechanisms (38–44). One commonly proposed mechanism for this is when a replication fork collides head on with an R-loop, and that fork stalls. The stalled fork is then cleaved or reverses to a chicken-foot structure, to generate a free DS end in an intermediate step towards repair and restart. However, these free DS ends can lead to fusion of two such stalled forks, resulting in chromosomal translocations (14–17,40–45). Another potential mechanism for DNA damage from R-loops is via DNA endonuclease cleavage of the opposing single strand (SS) DNA of the R-loop (16,40). For example, transcription-coupled repair nucleases can nick the opposing DNA SS, resulting in DSB formation when a replication fork collides with that nick. This can also lead to fusion of two such DSBs, again leading to chromosomal translocations (38,41–45). The fusions of DSB sites at unresolved R-loops may be a more common pathway to oncogenic chromosomal instability than previously appreciated (14–17,39–45).

The findings that mutations in several R-loop resolution components lead to life-threatening diseases also demonstrates that R-loop resolution is physiologically important for human health (14–17,46–55). For example, mutations in senataxin, a helicase that unwinds R-loops for resolution can cause oculomotor apraxia type 2 or amyotrophic lateral sclerosis type 4 (46–48). Mutations in the Fanconi anemia genes FANCA, FANCD2 and FANCM increase pathologic R-loop formation (49–52). BRCA1 plays a key role in resolving R-loops, and mutations in BRCA1 lead to breast and ovarian cancer (53–55). BRCA1 recruits the senataxin to R-loops, thereby preventing DNA DSB breaks and genomic instability (56). Thus, BRCA1-deficient cancer cells have increased R-loops and are sensitive to any further decrease in R-loop resolution (53–56). This implies that R-loops represent a potential target for synthetically lethal therapies in these cancers.

Multiple pathways have evolved to resolve R-loops, and these pathways overlap by sharing components. A key demonstration of this principle is BRCA1 and senataxin, whose RNA unwinding activity may be common to each resolution pathway (47,48,56). While it is likely that these R-loop resolution pathways have evolved to address specific types or locations of R-loops, the functional difference between pathways is not clear (14–17). An initial step in some R-loop resolution pathways may be unwinding of the annealed RNA from the DNA bubble, and there are multiple helicases that can accomplish this besides senataxin, including PIF1 DNA helicase (57) and DHX9/RNA helicase A, the latter of which is recruited to R-loops by TDRD3 (58,59).

There are also multiple types of RNases that can metabolize the annealed RNA strand of the R-loop, with or without RNA unwinding (14–17,58,59). For example, the most common R-loop resolution pathway centers on the ubiquitously expressed RNaseH1, which may be recruited to R-loops by RPA (60–63). The related RNaseH2 resolves R-loops only during G2/M, demonstrating strict cell cycle regulation, while RNaseH1 is active during the entire cell cycle (61). Interestingly, mutations in RNaseH2 cause the neurologic Aicardi-Goutières syndrome (62) while germline mutations in RNaseH1 are likely embryonic lethal (60). Another RNase R-loop resolution pathway centers on the yeast THO

and THSC complexes, which utilize RNA helicases for unwinding RNA:DNA duplexes in R-loops (14–17,64,65).

Interestingly, the unwinding and RNA degradation steps in R-loop resolution may be linked or these steps may resolve R-loops independently, although the circumstances defining linkage versus independence of these functions is not clear (14–17). Nonetheless, the multitude of overlapping components and pathways implies that resolving pathologic R-loops is of paramount importance to the cell (14–17). Thus, when R-loops are pathologically increased, such as with BRCA1-deficient cancers, the cell must marshal every resource at its disposal to survive (53–56).

MicroRNAs (miRs) are small RNAs with duplex stem-loop structures that regulate gene expression by binding to specific mRNAs to either mediate their degradation or to repress their translation (66,67). R-loops can regulate miR genomic loci transcription and promote the assembly of miR maturation complexes (68). There are several reports of miRs regulating expression of DNA repair factors (69,70), but little is known about whether specific miRs regulate R-loop resolution. In addition, while the generation of miRs is well defined, the regulation of their repression is less so. One mediator of repression of miRs is the unfolded protein response RNase, IRE1 known to promote digestion of tumor suppressor miRs in cancer (71,72). We previously reported that BRCA1 ubiquitinates IRE1, normally targeting it to the proteasome for degradation, and that in BRCA1-deficient cancers, IRE1 is markedly over-expressed (71).

In this study, we found that the constitutive over-expression of the RNase IRE1 in BRCA1-deficient cancer cells led to the repression of multiple miRs (71,72). Reconstituting the expression of one of these miRs, miR-4638-5p caused cell death in multiple types of BRCA1-deficient cells, but much less so in cognate BRCA1-repleted cells. Using an informatics search of mRNA 3′ UTRs we found that miR-4638-5p binds to several sites in the 3′ UTR of TATDN2 and represses its expression. We then demonstrated that TATDN2 is a structure-specific RNase that degrades the annealed SS RNA but not the bubble DNA in an R-loop. Depleting TATDN2 results in cellular R-loop accumulation, slowed replication and increased DNA damage and chromosomal instability in cancer cells with BRCA1-deficiency. These results suggest that BRCA1-deficient cells require TATDN2 for R-loop resolution, but wild type BRCA1-repleted daughter cells much less so. Thus, targeting TATDN2, perhaps by using miR-4638-5p could provide a therapeutic window to treat BRCA1-deficient tumors.

Materials and methods

Cell culture, transfection and survival assays

TATDN2, IRE1 and BRCA1 were selectively depleted by transient transfection of small interfering RNA (siRNA) using Lipofectamine RNAiMAX reagent (ThermoFisher, Waltham, MA). SMARTpool ON-TARGETplus, scrambled siRNA control (D-001810-10-20), TATDN2 SiRNA (L-020966-01-0005), IRE1 (L-004951-02-0005) and BRCA1 siRNA (L-003461-00-0005), were purchased from Horizon Discovery RNAi Technologies (Lafayette, CO). Two custom TATDN2 siRNAs AAGCACAACUGGAGCAGCA (NM_014760.4, nucleotides 25–43) and GAGGAAGCCUGCAGCCUUA (394–412) were also constructed by Horizon Discovery to ensure specificity of TATDN2 protein depletion and to overcome resistance of the HCC1937 BRCA1-mutant cells to the original TATDN2 siRNAs. All cell lines were obtained from the ATCC except the MDA-MB-436 and HCC1937 BRCA1-deficient and WT repleted cells, which were a gift from Dr. Junjie Chen (University of Texas MD Anderson Cancer Center, Houston, TX) and cultured per their specifications.

Briefly, the day prior to transfection, cancer cells (BRCA1-deficient MDA-MB-436 and its WT BRCA1 repleted derivative, BRCA1-deficient HCC1937, BRCA1-deficient UWB1.289 and BRCA1 WT MCF7 cells) were seeded at a density of 1.4×10^5 cells per well in a 6 well plate (73–77). Transfection reagents were prepared by slowly combining 6 μl of RNAiMAX/250 μl Opti-MEM (ThermoFisher Scientific) with 50 nM of siRNA/250 μl Opti-MEM at room temperature (RT) for 20 min before adding to cells. Between 4 h and 6 h after transfection, 0.5 ml of fresh medium containing 30% FBS was added to each well for all cell types. The DNA:lipid complex was removed 24 h post-transfection and replaced with complete growth medium. Cells were harvested 2 days post-transfection for colony formation (survival) assays, western analysis, immunofluorescence, or other assays. All experiments were performed at least three times in triplicate ($n \geq 9$). Clonal survival was determined by seeding transfected cells (MDA-MB-436 BRCA1$^{-/-}$ or repleted BRCA1^{+}, 800 cells; others, 1000 cells) per well in 6-well plates (71,73–77). Cells were incubated for 10–14 days, rinsed with PBS, fixed with 1% formaldehyde for 10 min and stained with 0.1% (w/v) crystal violet in methanol before colonies were counted. Colonies with >50 cells were counted as a surviving clone.

Western blot analysis

Protein expression of total TATDN2 was monitored by standard western blotting as we described (73–81). TATDN2 and β-actin antibodies were purchased from Millipore Sigma (St. Louis, MO; 05-636 and A2228, respectively). IRE1 antibody was purchased from Cell Signaling Technology (Danvers, MA; 3294) and IRE1-phospho S724 antibody was purchased from Abcam (Boston, MA; ab124945). Recombinant monoclonal S9.6 antibody was purchased from Absolute Antibody (Boston, MA, USA; ab01137-23.0), and 6X His-antibody was purchased from Bethyl Laboratories (Montgomery, TX). Secondary antibodies used for enhanced chemiluminescence (ECL) detection were rabbit IgG, HRP-linked Whole Ab (NA934-1ML) and HRP-conjugated mouse secondary antibody (Fisher Scientific, Pittsburgh, PA, NA931-1ML). Super-Signal West Pico Chemiluminescent Substrate was purchased from Fisher Scientific (34578) and Prometheus ProSignal ECL film (30–810L) was purchased from Genesee Scientific (El Cajon, CA).

MicroRNA quantitation assay

MiR-4638-5p was quantified using quantitative reverse transcriptase PCR as we previously reported (77). Global miR expression changes after IRE1 depletion was performed using microarray technology by LC Sciences (Houston, TX) on triplicate test (48 hours after transfection of siRNA against IRE1 in MDA-MB-436 BRCA1-mutant cells) and triplicate control cell samples (48 hours after transfection of scrambled siRNA).

SiRNAs used are listed above and transient transfection was carried out as described above.

Confocal immunofluorescent microscopy for DNA damage foci

Confocal microscopic immunofluorescence foci assays were performed as we previously described with minor modifications (73,74,76–78). In brief, MDA-MB-436, its WT BRCA1-repleted derivative, or MCF7 cells were cultured on coverslips followed by siRNA transfection. Cells were treated with the non-DNA damaging TOP2A inhibitor ICRF-193 (3 μM) for 10 h to induce mitotic stress from failed decatenation, and then fixed with either 4% formaldehyde for 10 min at ambient temperature or ice cold methanol at 4°C for 10 min (for R loop detection), rinsed three times with PBS and permeabilized with 0.1% Triton-X for 5 min at 4°C before incubation with γ-H2AX antibodies (Millipore Sigma, 05-636, dilution 1:200, St. Louis, MO), phospho-S4/S8 RPA32 antibody (Bethyl Laboratories, A300-245A), tubulin antibody (Abcam, ab64503), or recombinant monoclonal S9.6 antibody at 4°C overnight. The cells were then washed with PBS multiple times. Secondary antibodies (goat anti-mouse IgG, Alexa Fluor® 568 conjugate, A11004, dilution 1:400) (ThermoFisher Scientific, Carlsbad, CA) were added to the cells at ambient temperature and protected from light for 1 h. After washing thrice with PBS, coverslips were mounted in an anti-fade solution containing 4′,6-diamidino-2-phenylindole (DAPI). Samples were analyzed using either a Zeiss fluorescence microscope (LSM710, Carl Zeiss Microscopy, Thornwood, NY) or a Leica TCS SP5 confocal scanning microscope (Leica Microsystems, Exton, PA). Immunofluorescence images were captured with a Hamamatsu ORCA-ER digital camera (Hamamatsu Photonics K.K, Bridgewater, NJ) and processed by Zeiss Axiovision Release 4.6 software. Confocal images were processed with Leica LAS AF imaging software. Cells with ≥ 5 foci were scored as positive. Photomicrographs of distinct cell populations were taken at equal magnifications and equal fluorescence intensities. To assess nuclear structural abnormalities (retained micronuclei and post-mitotic bridging), MDA-MB-436 BRCA1-deficient cells, with or without TATDN2 depletion, were fixed as described above and stained with 300 nM DAPI (Beckman) in PBS for 5 min. After washing with PBS, coverslips were mounted in anti-fade solution and analyzed using confocal microscopy. Each confocal immunofluorescence assay was performed at least three times.

Mitotic arrest assays

ICRF-193 is a catalytic inhibitor of TOP2A that causes mitotic arrest due to entangled chromosomes from failed decatenation but not from DNA damage. Immunofluorescence of tubulin condensation into a mitotic spindle and 4′-6-diamidino-2-phenylindole (DAPI)–stained chromosome alignment in a metaphase plate was measured as we described (77,81). Interphase and metaphase-arrested cells were counted using immunofluorescence microscopy using a Zeiss confocal fluorescence microscope with a 63× objective equipped with laser and filter settings for DAPI, FITC and Texas Red. Increased mitotic cells after ICRF-193 exposure reflects mitotic decatenation arrest. Each experiment was performed in triplicate, with >100 cells counted per condition.

Analysis of post-mitotic chromosomal segregation defects

We assessed chromosomal structural abnormalities (post-mitotic retained chromosomes seen as micronuclei and shared chromosomes seen as chromosome bridging) were scored using confocal immunofluorescent microscopy as we previously described (74,77). Control or treated cells were grown on coverslips and fixed as described above, and stained with 300 nM DAPI (Beckman) in PBS for 5 min. After washing thrice with PBS, coverslips were mounted in anti-fade solution and analyzed within 24 h on a Zeiss fluorescence microscope (Axiovert 200 M). Each immunofluorescence assay was performed at least 3 times, each with triplicate slides.

DNA fiber analysis of replication fork progression and restart

DNA fiber analysis for measuring stalled replication fork repair and restart was performed as we previously described (71,73,74,76,77,80). Briefly, 6×10^5 MDA-MB-436 cells were incubated overnight at 37°C in 6-well plates, then treated with 100 mM chloro-deoxyuridine (CldU) and 100 nM ARV-825 to increase R-loops (82) or vehicle control for 6 h at 37°C. The CIdU/ARV-825 medium was removed, cells were washed in fresh medium, and then treated with 20 mM Iodo-deoxyuridine (IdU) for 1 h at 37°C. Cells were harvested and resuspended in PBS at 2×10^5 cells/ml and agarose plugs were made for DNA fiber analysis.Cells were mixed with a low melting agarose to make agarose plugs. Agarose plugs were chilled at 4°C for 30 min to solidify the agarose. Each plug was mixed with 200 μl 0.5 M EDTA, 25 μl sarkosyl, and 50 μl proteinase K and incubated at 50°C for 18 h. Plugs were washed three times with TE buffer (10 mM Tris–HCl, pH 8, 1 mM EDTA) at RT and placed in a reservoir containing 1 ml of MES buffer (pH 5.5). Reservoirs containing agarose plugs were incubated at 65°C for 30 min to melt agarose. The melted agarose was digested with 2 μl of agarase (New England Biolabs) at 42°C for 14–18 h. After digestion with agarase, these reservoirs were stored at 4°C for 2–3 days before processing for DNA fibers. DNA fibers were processed on slides (GenomicVision) using the FiberComb molecular combing system (Genomic Vision) to ensure uniform DNA combing. The newly synthesized CldU and IdU tracks were labeled (for 2.5 h in the dark, at RT) and detected with antibodies recognizing CldU and IdU, followed by 1 h incubation with secondary antibodies at RT in the dark. Slides were mounted in PermaFluor aqueous self-sealing mounting medium (ThermoFisher Scientific), and images of DNA fibers were captured with a confocal Olympus FV1000D scanning microscope (Olympus America Inc., Center Valley, PA). DNA fiber images were analyzed using ImageJ software (https://imagej.net/ij/index.html). At least 200 fibers were quantified for each experiment.

TATDN2 protein purification

WT and mutant versions of TATDN2 were purified from HEK-293T cells stably expressing histidine-tagged TATDN2 as we described (75,76,79,80) with modifications as described here. Three mutants of TATDN2 were generated, E593A, E705A and D707A as we described (80). 6X His-tagged TATDN2 was detected in cell extracts by Western blotting using anti-6X His and anti-TATDN2 antibodies. Cells over-

expressing WT or mutant TATDN2 were suspended in 20 ml of ice cold Buffer A (50 mM Tris–HCl, pH 7.5, 5 mM DTT, 0.5 M NaCl, 1 mM $MgCl_2$, 0.4% nonidet-P40, 10% glycerol, 1 mM EDTA, 1 mM PMSF and 20 mM Imidazol) for lysis, and then centrifuged at 100 000 × *g* for 30 min. Supernatants were filtered through Whatman paper and incubated at 4°C for 60 min with nickel-NTA affinity gel pre-equilibrated with Buffer B (25 mM Tris–HCl, pH 7.5, 0.5 M NaCl, 5% glycerol, and 20 mM Imidazol). The beads were then washed 10 column volumes with Buffer B containing 2 M NaCl prior to protein elution. TATDN2 wild-type protein was eluted with buffer C (25 mM Tris–HCl, pH 7.5, 0.5 M NaCl, 5% glycerol, and 150 mM Imidazol). Fractions containing TATDN2 were pooled and dialyzed to remove NaCl and imidazole. The dialysis buffer D was composed of 25 mM Tris pH 7.5, 50 mM NaCl, 10% glycerol and 1 mM DTT. The eluted protein was further diluted in dialysis buffer and then loaded onto a heparin-Sepharose 6 column (Cytiva, Marlborough, MA) pre-equilibrated with buffer F (25 mM Tris, 50 mM NaCl, 5% glycerol, 0.2 mM TCEP pH 7.9) in order to isolate it from the protein chaperone HSP70, which co-eluted with human TATDN2 from the nickel-NTA beads. After washing the column, TATDN2 protein was fractionated using high pressure liquid chromatography in a linear salt gradient (0–2 M NaCl) in buffer D. The eluted protein was characterized by Coomassie staining and western blot analysis followed by dialysis against the above dialysis buffer and stored at −80°C.

Single cell DNA electrophoresis (alkaline comet) assay

Alkaline single cell electrophoresis assays for DNA damage and repair were performed using the Comet Assay kit (Trevigen, Gaithersburg, MD, USA) as we described (74,76). Briefly, MDA-MB-436 cells were transfected with siRNA-Scr (Scrambled) control siRNA or siRNA-TATDN2 as described above. Twenty-four hours later, cells were protected from light, trypsinized, counted and adjusted to 1 × 10^5 cells/ml in PBS. Approximately 2000 cells were premixed with molten agarose and seeded into each well on a Comet slide. Slides were subjected to electrophoresis in the dark. After electrophoresis slides were processed, DNA was stained with SYBR green dye and images were captured using a fluorescence microscope (Zeiss Axiovert 200M, Thornwood, NY) at 10X magnification. Tail length was calculated using ImageJ software with the OpenComet plug-in.

Kinetoplast DNA decatenation assay

Purified recombinant TATDN2 and its mutant proteins were tested for the decatenation activity using kinetoplast catenated DNA (kDNA) relaxation assay as we described (81). Purified recombinant TopoIIα and catenated kDNA were used as a positive control, based on the manufacturer's instructions (Topogen, Buena Vista, CO). Increasing amounts of purified TATDN2 were incubated with kDNA in the manufacturer's buffer for 1 h at 37°C. KDNA nicking was visualized on 1% agarose gel electrophoresis in ethidium bromide and quantified by densitometry using ImageJ software (81).

R-loop resolution assays

R-loop resolution assays were performed as we described (83) using these oligonucleotides:

D1	CATTGCATATTTAAAACATGTTGGATCCCACGTT GCATGCTGATAGCCTACTAGAGCTGTATGAATTC AAATGACCTCTTATCAAGTGAC
Cy5-D1	Cy5-CATTGCATATTTAAAACATGTTGGATCCCA CGTTGCATGCTGATAGCCTACTAGAGCTGTATGA ATTCAAATGACCTCTTATCAAGTGAC
D2	GTCACTTGATAAGAGGTCATTTGAATTCATGGCT TAGAGCTTAATTGCTGAATCTGGTGCTGGGAT CCAACATGTTTTAAATATGCAATG
D3	GCACCAGATTCAGCAATTAAGCTCTAAGCC
R1	GUGCUACGAUGCUAGUCGUAGCUCGGGAGUGC ACCAGAUUCAGCAAUUAAGCUCUAAGCC
R2	GCACCAGAUUCAGCAAUUAAGCUCUAAGCCGC UGACGGCUCGAUGCUGAUCGUAGCAUCG
R3	GCACCAGAUUCAGCAAUUAAGCUCUAAGCC

The relevant oligomer was labeled with γ-^{32}P-ATP (6000 Ci/mmol, 10 μCi/μl, 2 μl) using T4 polynucleotide kinase (20 U) in 50 mM Tris–HCl pH 7.5, 10 mM $MgCl_2$ and 5 mM DTT in 20 μl total volume at 37°C for 1 h, then samples were purified using a micro-Biospin 6 column. To generate an R-loop with a 5′-RNA overhang, D1 + D2 + R1 were annealed, with R1 labeled. To generate an R-loop with a 3′-RNA overhang, D1 + D2 + R2 were annealed, with R2 labeled. To generate an R-loop with no RNA overhang, D1 + D2 + R3 were annealed, with R3 labeled. To generate an RNA:DNA hybrid, D3 + R3 were annealed, with R3 labeled. To generate a D-loop, D1 + D2 + D3 were annealed, with D3 labeled. Oligonucleotides (1 pmole each) were annealed in 10 mM Tris–HCl pH 7.5, 50 mM NaCl in 20 μl total volume by heating to 95°C for 10 min in a PCR machine, and then gradually decreasing the temperature to 10°C by 1°C/min. Annealed oligonucleotides were checked for proper annealing by loading 5 fmol of annealed products on a native 10% polyacrylamide gel with 1 × TAE at 100 V for 60 min. Correct annealing of oligonucleotides was verified based on differences in electrophoretic mobility of single, duplex and triplex oligonucleotides. The DNA bubble structure was generated by annealing Cy5-D1 + D2, and the annealing verified by mobility shift by running next to Cy5-D1 in 10% TAE-polyacrylamide gel. R-loop assays were performed in a buffer with 30 mM Tris–HCl, pH 7.5, 50 mM KCl, 5 mM divalent cation (Mg^{2+}, Mn^{2+} or Ca^{2+}), 0.25 mg/ml BSA, 5% glycerol, 0.01% NP-40, 1 mM DTT, with 2 nM nucleic acids substrate and 12.5–50 nM concentrations of purified TATDN2 protein in 10 μl reactions incubated at 37°C for 30 min. Reactions were stopped by adding 1 μl of 1% SDS and 1 μl of 10 mg/ml proteinase K and incubating at 37°C for 5 min. Finally, 2 μl of 10 × loading buffer (100 mM Tris–HCl, pH 7.5, 10 mM EDTA, 50% glycerol, 0.15% Orange G) was added to the reaction. Assessment of specific R-loop RNA metabolism was performed using both native and denaturing polyacrylamide gel electrophoresis. For native gel electrophoresis, the Mini-PROTEAN Tetra apparatus (Bio-Rad, Hercules, CA) was immersed in an ice bath to maintain low temperature during electrophoresis. Native reaction mixes (7 μl) were loaded on a native 10% Tris-Acetate-EDTA (TAE) polyacrylamide gel (10.1 × 7.3 cm, 1.5 mm thick, 37.5:1) and run at 100 V until the dye front reached 3/4th of the gel. Heat-denatured radiolabeled substrate was used as a marker. For denaturing gel electrophoresis, 10 μl 2× formamide dye (95% formamide, 5 mM EDTA, 0.025% (w/v) Orange-G dye) was added to each reaction mixture, and denatured at 95°C for 5 min. Six μl of the reaction mix was

loaded onto each well of a polyacrylamide sequencing gel (45 cm × 33 cm × 0.2 mm) in 1X Tris-Borate-EDTA (TBE) buffer and run at a constant 75 W for 2 h. After electrophoresis, the polyacrylamide sequencing gel was immersed in fixing solution (50% methanol, 20% polyethylene glycol 400) for 15 min. Gels were placed on a sheet of Whatman paper, covered with plastic wrap and dried under vacuum at 80°C for 1 h. The dried gels were exposed to a phosphor screen overnight, the screens were scanned in Typhoon phosphorimager (GE), and the band intensities quantified using image analysis software (ImageQuant TL 8.0, GE Healthcare). The percentage of product formation was calculated using the formula: product × 100/(substrate + product).

DNA:RNA immunoprecipitation (DRIP) quantitative polymerase chain reaction (qPCR)

DRIP-qPCR was performed as previously described (84). Briefly, TATDN2 was depleted as above in quadruplicate plates each containing at least 8 million BRCA1-mutant or WT-repleted MDA-MB-436 cells, with scrambled siRNA serving as a control. DRIP-qPCR assays were performed by immunoprecipitating DNA:RNA hybrids using the S9.6 antibody (Kerafast, Boston, MA) from gently extracted and enzymatically digested DNA with the following cocktail of restriction enzymes: HindIII, EcoRI, XbaI, SspI and BsrGI, treated or not with RNase H (New England Biolabs) *in vitro* as described (85). The immunoprecipitated DNA was recovered using phenol/chloroform/isoamyl alcohol (25:24:1), centrifuged to recover DNA and allowed to air-dry prior to resuspending in RNase-free TE buffer. The relative abundance of DNA–RNA hybrid immunoprecipitated in each region was normalized to the input values and the scrambled siRNA control as needed (86). QPCR primers for the APOE gene locus and the negative control EGR-1 locus were as follows in 5′-3′ direction: APOE (F: CCGGTGAGAAGCGCAGTCGG; R: CCCAAGCCCGACCCCGAGTA), EGR-1 (F: GAACGTTCAGCCTCGTTCTC; R: GGAAGGTGGAAGGAAACACA). DRIP-qPCR assays were performed in technical quadruplicates for each immunoprecipitation 72 h after siRNA transfection as described (85).

Mass spectrometry analysis of TATDN2 complex

Mass spectrometry (MS) analysis of proteins associated with TATDN2 after DNA damage was performed by isolating nuclear proteins from U2OS cells expressing Myc-tagged TATDN2 as we and others described previously with some modifications (78,87). Two days after transfecting U2OS cells with either Myc-TATDN2 or pCMV using Lipofectamine 3000 (ThermoFisher), ∼80 × 10^6 cells per condition were exposed to 10 Gy of ionizing radiation using a ^{137}Cs Faxitron MultiRad 225 irradiator (Precision Xray; 110 kV, 11 mA, 0.50 mm aluminum filter, 40 cm from the source), and incubated for 1 h to recover. Cells were harvested and suspended in hypotonic Buffer (10 mM HEPES pH 7.9, 10 mM KCl, 0.1 mM EDTA, 1 mM dithiothreitol (DTT), with a mixture of protease and phosphatase inhibitors (Millipore Sigma) for 15 minutes, then 10% IGEPAL (Millipore Sigma) was added to a final concentration of 0.5%. Cells were vigorously vortexed for 1 min at RT, and cell suspensions were centrifuged for 10 min at 1000 × *g*. The cytoplasmic fraction was removed, the nuclear pellet was washed with ice-cold PBS, and resuspended in ice-cold lysis buffer (20 mM HEPES pH 7.9, 400 mM NaCl, 1 mM EDTA, 1 mM DTT, with protease and phosphatase inhibitors). Salt reducing buffer (20 mM HEPES pH 7.9, 1mM EDTA) was added to dilute NaCl to a final concentration of 150 mM and samples were centrifuged at 24,000*g* for 2 h at 4°C. Nuclear extracts were pre-cleared using Binding Control magnetic agarose beads (Proteintech, Rosemont, IL) at 4°C for 45 min, then Myc-TATDN2 was immunoprecipitated overnight using Myc-Trap magnetic agarose (Proteintech) at 4°C. The beads were washed five times with the 150 mM NaCl lysis buffer, and polypeptides were eluted with Laemmli buffer (Bio-Rad, Hercules, CA). Samples were run on a 7.5% Mini-PROTEAN TGX Stain-Free gel (Bio-Rad) until they were approximately 3 cm into the resolving gel. The gel was stained with Pierce Coomassie Brilliant Blue Dyes for 1 h at RT, then washed with deionized distilled H_2O three times for 1 h each. The gel lanes were cut with clean razors to 1 mm cubes and further processed by the mass-spectrometry proteomics facility at UT Southwestern Medical Center, Dallas, TX. Multiple controls (cell lysates with other Myc-tagged proteins) were processed at the same time and immunoprecipitated in parallel to exclude common non-specific binders. Gel fragments were digested overnight with trypsin (Pierce, Appleton, WI) following reduction and alkylation with DTT and iodoacetamide (Sigma). Sample cleanup was performed by solid-phase extraction with an Oasis HLB plate (Waters, Milford, MA) and the resulting samples were injected onto a QExactive HF mass spectrometer coupled to an Ultimate 3000 RSLC-Nano liquid chromatography system. Samples were injected onto a 15-cm long EasySpray column (i.d 75 μm, ThermoFisher Scientific) and eluted with a gradient from 100:0% buffer A:buffer B to 72:28% buffer A:buffer B over 90 minutes with a flow rate of 250 nl/min. Buffer A contained 2% (v/v) acetonitrile (ACN) and 0.1% formic acid in water, and buffer B contained 80% (v/v) ACN, 10% (v/v) trifluoroethanol and 0.1% formic acid in water. The mass spectrometer operated in positive ion mode with a source voltage of 2.5 kV and an ion transfer tube temperature of 275°C. MS scans were acquired at 120 000 resolution in the Orbitrap and up to 20 MS/MS spectra were obtained for each full spectrum acquired using higher-energy collisional dissociation for ions with charges of 2–8. Dynamic exclusion was set for 20 s after an ion was selected for fragmentation. Raw mass spectrometry data files were analyzed using Proteome Discoverer v.3.0 (ThermoFisher), with peptide identification performed using Sequest HT searching the UniProt human protein database. Fragment and precursor tolerances of 10 ppm and 0.02 Da were specified, and three missed cleavages were allowed. The false-discovery rate cutoff was 1% for all peptides. The .RAW data file, .mgf peak list and the Excel spreadsheet has been uploaded to MassIVE, Accession Number: MSV000092192.

Statistical analysis

All experiments were performed at least 3 times or more and no results were excluded from statistical analysis. Statistical analysis was performed using two-way analysis of variance (ANOVA) by using SigmaPlot 13 (Systat Software, San Jose, CA). A one-tailed t-test was used to determine significant differences between control and treated groups. The criterion for statistical significance was $P \leq 0.05$ and for each figure statistical significance has been indicated as $^*P<0.05$,

$^{**}P<0.01$, $^{***}P<0.001$, $^{****}P<0.0001$. For western blotting data, band intensities were measured using ImageJ and normalized to the loading controls (β-actin).

Results

MiR-4638-5p targets TATDN2 and is lethal for BRCA1-deficient cells

We previously reported that the unfolded protein response RNase IRE1 is over-expressed and constitutively phosphorylated in BRCA1-deficient cells (71). Phosphorylated IRE1 can degrade miRs as well as messenger (m) RNAs to promote the unfolded protein response (71,72). We first confirmed the over-expression and increased phosphorylation of IRE1 in the BRCA1-deficient MDA-MB-436 cells (Figure 1A). Depleting IRE1 in MDA-MB-436 cells resulted in increased levels of many miRs listed in Supplementary Figure S1, as defined by microarray analysis. One such miR whose expression was increased after IRE1 depletion was miR-4638-5p. Using Q-PCR assays, we found that miR-4638-5p was more highly expressed in BRCA1-deficient but not WT BRCA1-repleted MDA-MB-436 cells (Figure 1B), which has lower IRE1 levels and phosphorylation (71). We previously reported that IRE1 depletion is synthetically lethal in BRCA1-deficient but much less so WT BRCA1-repleted MDA-MB-436 cells (71). We hypothesized that this synthetic lethality was due to increased miR expression that repressed proteins harmful to the BRCA1-deficient cells. We found that depleting IRE1 resulted in increased miR-4638-5p expression and that reconstituting miR-4638-5p expression is synthetically lethal in BRCA1-deficient but not WT BRCA1-repleted cells as measured by clonal colony survival assays (Figure 1C).

We performed an informatics search for mRNA binding sites for miR-4638-5p that might explain its selective synthetic lethality in BRCA1-deficient cancer cells. We found that it had multiple binding sites in the 3′ UTR of an uncharacterized nuclease termed TATDN2, one of three human members of the TATD family, related to the bacterial TatD nuclease (1–3). MiR-4638-5p predicted binding sites in TATDN2 mRNA (NM_014760.4) were at the following locations, in descending order of predicted strength of the interaction:

3231–3259 (AUUCUGUUCUCUGCAGCCUGUUUUUGAGU)
3834–3854 (CUUUGUGUACCCCGCCCAGGU)
4758–4778 (AUUUAUGUGCUGUUGCACAGU)
3285–3310 (ACUUGUCUAAGCACAUGUGGGUGUGU)
4039–4065 (UCUCCUUCACCUUUUGAGCAACUGAGU)

The first binding site starting at 3231 has a significantly stronger predicted interaction with miR-4638-5p than the others, at -21.4 kcal/mol (Figure 1D).

We next tested whether the interaction between miR-4638-5p and the TATDN2 3′ UTR could result in functional repression of protein translation. We found that reconstituting miR-4638-5p in MDA-MB-436 cells repressed expression of TATDN2 protein and decreased expression of a luciferase reporter bearing the 3′ UTR of TATDN2 (Figure 1D). Consistent with the reconstitution of miR-4638-5p being synthetically lethal for BRCA1-deficient MDA-MB-436 cells, depletion of TATDN2 in BRCA1-deficient cell lines MDA-MB-436 and HCC1937 (breast cancers) and UWB1.289 (ovarian cancer) was indeed synthetically lethal (Figure 1E). In contrast, WT BRCA1-repleted MDA-MB-436 cells were affected far less than BRCA1-defective parent cells (Figure 1E), implying a potentially significant therapeutic window if TATDN2 could be successfully targeted. These data also indicate that the repression of miR-4638-5p by IRE1 in BRCA1-mutant cells is important for their survival, and that one target of miR-4638-5p is TATDN2.

TATDN2 is an RNA 3′ exonuclease and endonuclease

Protein Atlas confocal immunofluorescence demonstrates that the majority of human TATDN2 localizes to the nucleus in a speckled pattern (https://www.proteinatlas.org/ENSG00000157014-TATDN2/subcellular). We purified recombinant human TATDN2 protein from HEK293T cells using a 6X His tag and nickel-NTA column followed by high performance liquid chromatography (HPLC) using a heparin column. The HPLC step was required to separate TATDN2 from HSP70, which co-purified with TATDN2 on the nickel-NTA column (Supplementary Figure S2). Previous studies indicated that bacterial TatD was a magnesium ion-dependent 3′ exonuclease preferential for SS RNA or DNA (1–3). We tested TATDN2 activity on an RNA hairpin structure and found that it had strong 3′ RNA exonuclease and endonuclease activities (Figure 2A) (5–7). TATDN2 both sequentially clipped off the 3′ RNA end and cleaved internally in the DS region of the RNA hairpin. This activity was reaction time-dependent (Figure 2A) and was significantly greater than its activity on DNA (see below). At higher TATDN2 concentrations, the 3′ exonuclease clipping appears reduced. It is unlikely that either activity has changed due to concentration-rather, the increasing concentration results in more endonuclease cleavage, which results in smaller fragments containing the 3′ end, which would run at a faster rate on the gel.

Based on the TATDN2 RNA hairpin activity and its unique nuclease catalytic domain (Figure 2A, B), we hypothesized that TATDN2 might also resolve R-loops, given their RNA–DNA hybrid structure. We tested this hypothesis with purified human TATDN2 on multiple radiolabeled R-loop structures using *in vitro* biochemical reconstitution and native and denaturing gel electrophoresis assays. We found that WT recombinant purified TATDN2 specifically degraded the RNA strand but not the DNA strands of an R-loop, independent of whether there was a 5′ or 3′ RNA overhang, or no RNA overhang (Figure 2C–E). Based on analysis of the Alphafold-2 tertiary structure of human TATDN2, the reported structures of human TATDN1 and 3, and the reported tertiary structure of bacterial TatD, we predicted that three amino acids in the catalytic domain, E593, E705 and D707, could possibly chelate two divalent cations (Figure 2B) (1–4). We mutated each of these individually to alanine in purified recombinant TATDN2 protein and tested these variants in the R-loop biochemical reconstitution assay. We found that E593A and E705A completely abrogated degradation of RNA in the R-loop while D707A retained a low level of activity (Figure 2C–E). Chen *et al.* (2) reported that *E. coli* TatD E91A, E201A and D203A, which correspond to human TATDN2 E593, E705 and D707, respectively, are catalytically defective. This is consistent with our biochemical data, except the D707A mutant retained limited R-loop resolution activity, unlike the full abrogation of this activity with E593A and E705A mutations.

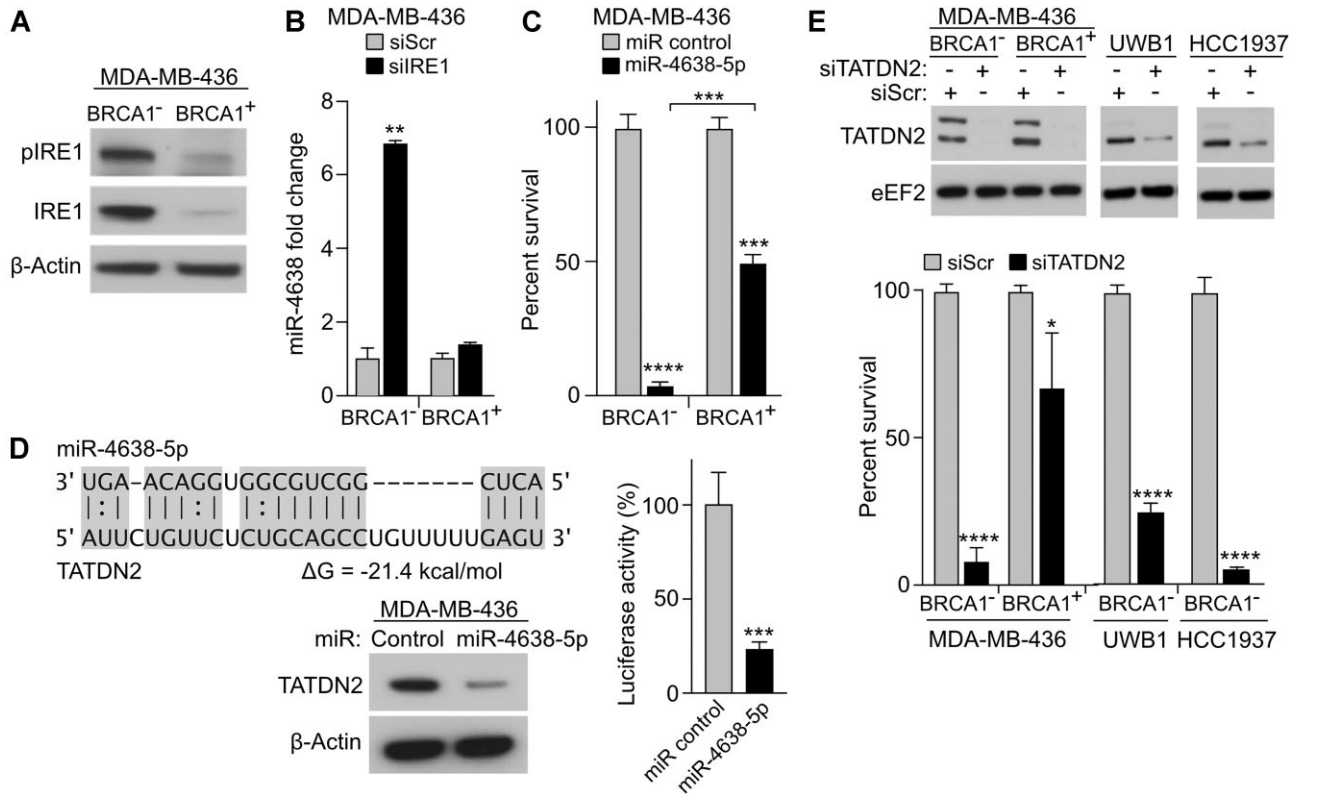

Figure 1. MiR-4638-5p reconstitution in BRCA1-deficient cells results in synthetic lethality. (**A**) The RNase IRE1 (both total and phosphorylated) is constitutively over-expressed in BRCA1-deficient MDA-MB-436 cells. (**B**) Depleting IRE1 results in increased levels of miR-4638-5p in BRCA1-deficient but not WT BRCA1-repleted MDA-MB-436 cells. (**C**) Reconstituting miR-4638–5p expression is synthetic lethal in BRCA1-deficient but not WT BRCA1-repleted cells. (**D**) miR-4638-5p has high affinity binding sites in the 3′ UTR of TATDN2 (position 3231 to 3259 in NM_014760.4). Western blot demonstrates miR-4638-5p regulates the expression of TATDN2. Transfection of miR-4638-5p in MDA-MB436 cells represses luciferase activity when the reporter contains the 3′ UTR of TATDN2. (**E**) Depletion of TATDN2 in the BRCA1-deficient MDA-MB-436, HCC1937 (breast cancer) and UWB1.289 (ovarian cancer) cell lines generate synthetic lethality, but 8-fold less of an effect is seen in BRCA1-repleted MDA-MB-436 cells. Western analysis demonstrates depletion of TATDN2, which has two isoforms in some cell lines, both specifically depleted. For all figures, $*P < 0.05$, $**P < 0.01$, $***P < 0.001$, $****P < 0.0001$.

TATDN2 specifically degrades the RNA strand of an R-loop

Previous reports indicate that bacterial TatD is a magnesium ion-dependent 3′ exonuclease preferential for SS RNA or DNA (1–3). Consistent with bacterial TatD (2), human TATDN2 required a divalent cation for activity, with maximal activity occurring with Mg^{2+}, mild activity with Mn^{2+} and very limited activity with Ca^{2+} (Supplementary Figure S3A–D). These assays also revealed TATDN2 R-loop binding as a supershift on the native gels. This supershift is only seen when the Mg^{2+} ion is lacking; otherwise the R-loop is digested by TATDN2 (Supplementary Figure S3D, E).

Based on the supershift seen in the native gel R-loop cleavage assays when the required divalent cation is missing, we investigated WT TATDN2, E593A TATDN2 and N-terminal truncated (490–761) TATDN2 binding to R-loops (Figure 3) using electrophoretic mobility shift assays (EMSA). We showed significant R-loop binding by WT TATDN2 that was eliminated by treatment with proteinase K and SDS (Figure 3A). The catalytically-defective E593 mutant showed limited R-loop binding, and binding was abrogated in the truncation mutant, TATDN2 (490–761), that lacks the long N-terminal disordered region (Figure 3A,B). The K_d for WT TATDN2 binding to R-loops is 19 nM.

We next examined the activity of TATDN2 on D-loops and RNA:DNA DS duplexes and compared that to its R-loop metabolism activity. In contrast to its robust R-loop resolution activity, TATDN2 showed no activity against a D-loop (SS DNA hybridized to a DNA bubble), and minimal activity against the RNA strand of an RNA–DNA hybrid duplex oligomer (Figure 4A, B), indicating that it prefers the RNA of an R-loop as a substrate. Using denaturing gel electrophoreses to measure fractions and sizes of degraded products, we found that TATDN2 specifically degraded the RNA strand of an R-loop from the 3′ end (Figure 4C, D). Although R-loop binding was not detected with the N-terminal truncated TATDN2 (490–761) (Figure 3), it still had minimal R-loop resolution activity in the more sensitive denaturing gel enzymatic RNA digestion assay, 7-fold worse than WT TATDN2 (Supplementary Figure S4).

It is likely that TATDN2 degrades the RNA strand of an R-loop from the 3′ end for two reasons; first, if TATDN2 has 5′ exonuclease activity then we would have seen only single labeled nucleotides in the R-loop denaturing gels, given that the RNA probe is labeled at the 5′ end (Figures 2 and 4). Second, we would have seen only single nucleotides in the cleavage of the hairpin RNA, which was labeled at the 5′ end as well (Figure 2). Instead, we see larger cleaved products in a ladder for both assays.

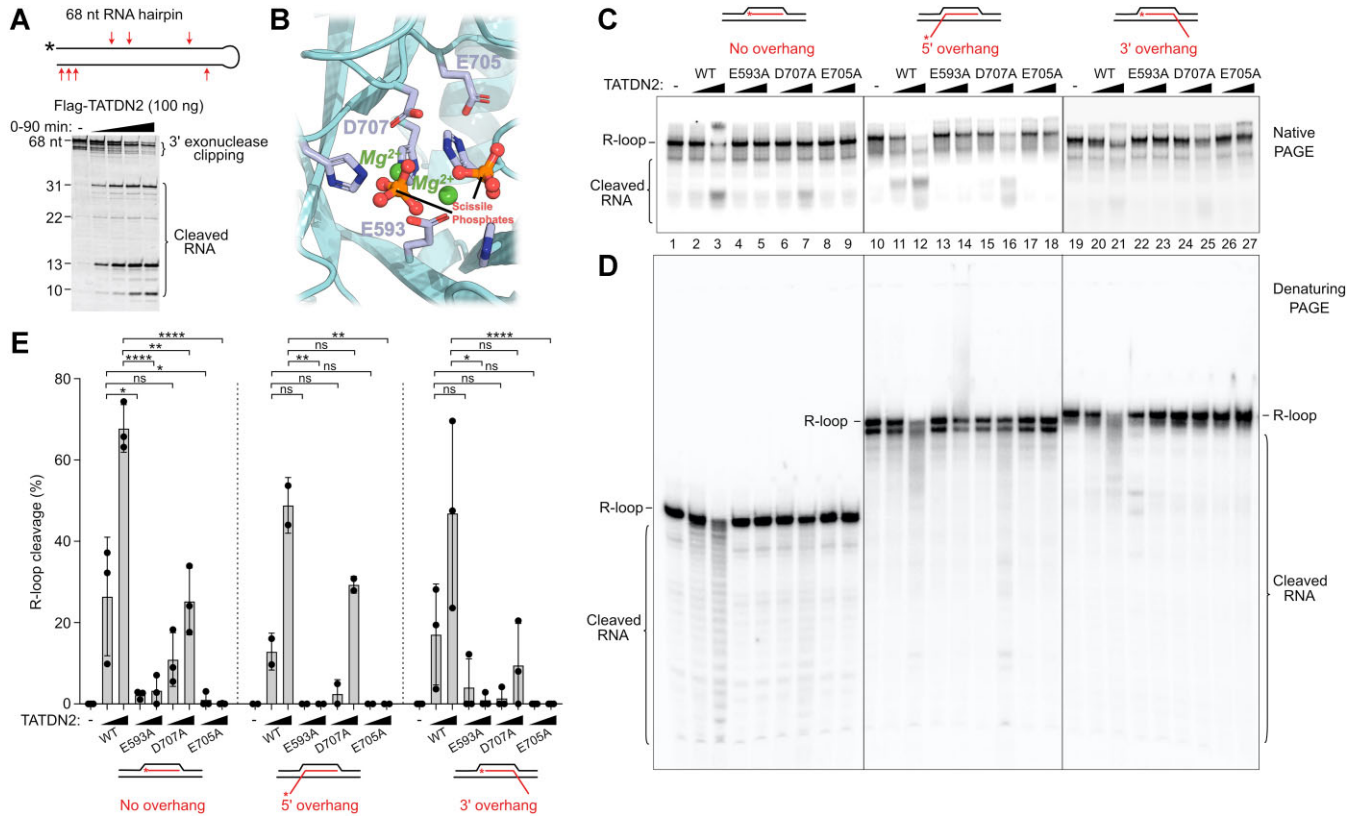

Figure 2. TATDN2 is a structure-specific RNase. (**A**) Schematic of 68 nt RNA hairpin (above) and denaturing gel ribonuclease assay (below) showing TATDN2 RNA hairpin 3′ exonuclease and endonuclease activity. Arrows indicate approximate cleavage positions in RNA hairpin. (**B**) The three-dimensional structure of TATDN2 catalytic site predicted by AlphaFold and by comparison to bacterial TatD and human TATDN1 and 3 (2,4), showing the acidic amino acids predicted to chelate the required divalent cation essential for nuclease activity of all DNaseI family members. (**C, D**) Activity of recombinant TATDN2-WT, E593A, D707A, E705A mutant proteins on R-loops without an RNA overhang (lanes 1–9), with a 5′ RNA overhang (lanes 10–18), or with 3′-RNA overhang (lanes 19–27); products separated in a native polyacrylamide gel (C) or denaturing polyacrylamide gel (D) to assess the fraction and size of cleaved RNA products from R-loops. E593A and E705A mutations in TATDN2 protein lack R-loop RNA exonuclease activity, while the D707A mutant has decreased activity. (**E**) Quantitation of R-loop activity expressed as a percentage of cleaved RNA in R-loops ($n = 3$).

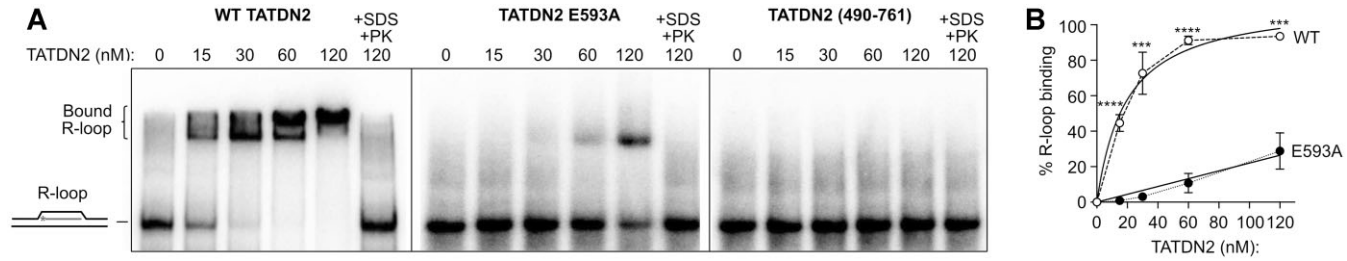

Figure 3. TATDN2 R-loop binding. (**A**) WT, E593A and N-terminal truncated (490–761) TATDN2 were incubated with an R-loop substrate and binding was determined by EMSA. (**B**) Plot of WT and E593A mutant TATDN2 R-loop binding measured by scanning densitometry. The Kd for WT TATDN2 is 19.3 nM; K_d was not calculated for the weakly binding E593A mutant, nor the non-binding 490–761 truncation mutant.

We next tested the activity of TATDN2 against various DNA substrates (Supplementary Figure S5). We found that it had little DNA nuclease activity against any SS or DS substrate. TATDN2 had no 3′ or 5′ exonuclease activity, no uracil glycosylase activity, and no 5′ flap endonuclease activity on DNA substrates (Supplementary Figure S5A–C). In contrast to TATDN1 and 3, it has only very weak abasic endonuclease activity, detected with high TATDN2 concentrations and prolonged autoradiogram exposure (Supplementary Figure S5D) (4). However, as noted above and discussed later, the nuclease domain of TATDN2 has distinct differences from TATDN1 and 3.

Interestingly, we found that TATDN2 had nicking activity on catenated kDNA, relaxing the supercoils to open circle DNA and linear DNA (Supplementary Figure S6), consistent with a previous report that zebrafish TATDN1 nicks catenated DNA (12). The E593A human TATDN2 species lost its decatenation capability, indicating this activity is not a contaminant. Loss of the amino terminal enhanced decatenation activity (Supplementary Figure S6), implying that it negatively regulates catenated DNA nuclease activity. TATDN2 had no nucleolytic activity on duplex DNA containing a bubble, a structure similar to an R-loop without the RNA (Supplementary Figure S7). Together these results indicate that TATDN2

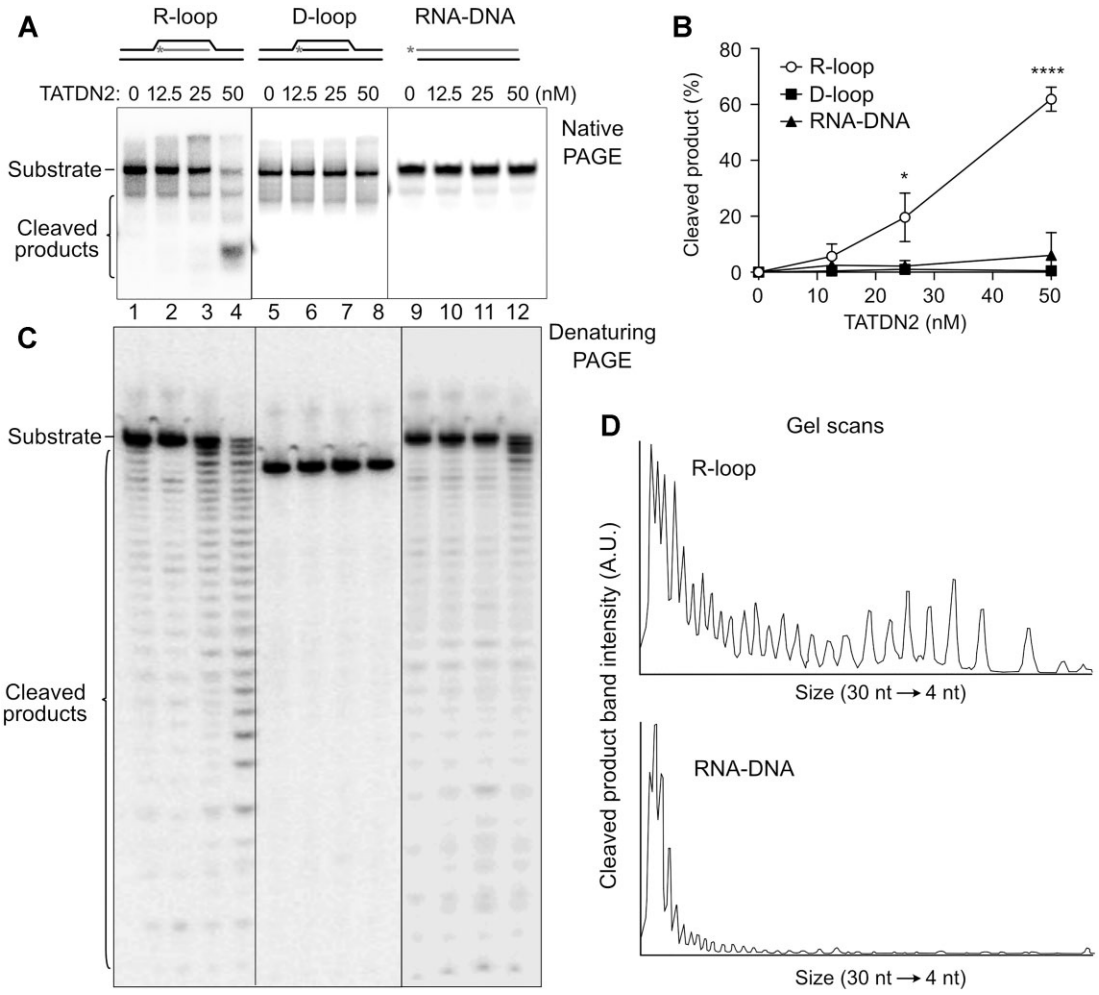

Figure 4. TATDN2 is specific for RNA in R-loops. (**A**) TATDN2 activity on R-loops (lanes # 1–4), D-loops (lanes # 5–8) and RNA–DNA duplexes (lanes # 9–12) was analyzed in a native gel. TATDN2 nucleolytic activity is specific for RNA in a R-loop substrate. (**B**) Quantitation of cleaved products from scans of gels as in panel A ($n = 3$). Statistics are shown for R-loop versus RNA–DNA duplex. (**C**) TATDN2 R-loop cleavage products resolved by size in a denaturing gel. (**D**) Quantitation of the cleaved RNA in R-loop (lane #4 of panel C) and RNA–DNA duplex (lane #12 of panel C); gel scan images were generated with ImageJ. TATDN2 only has RNase activity on R-loops, not D-loops or RNA–DNA hybrids.

preferentially degrades RNA in R-loop structures, rather than generic RNA–DNA hybrids, D-loops, or DNA bubble structures.

TATDN2 promotes R-loop resolution *in vivo*

BRCA1 is important for resolution of R-loops, and cancers with BRCA1-deficiency have difficulty resolving R-loops and further compromise of R-loop resolution in these cells causes synthetic lethality (53–56). We next used confocal immunofluorescence to examine whether TATDN2 depletion increased cellular R-loops in BRCA1-deficient and WT BRCA1 repleted MDA-MB-436 cells. Consistent with previous reports, we found that lack of BRCA1 resulted in more nuclear R-loops being detected by immunofluorescent staining with the R-loop-specific S9.6 antibody in the BRCA1-deficient MDA-MB-436 cells (Figure 5A, B). We found that R-loops were markedly increased after TATDN2 depletion in both the BRCA1-deficient and the WT repleted cells, but the BRCA1-deficient cells had relatively more R-loops after TATDN2 depletion than the WT repleted cells (Figure 5A, B).

Genomic DNA containing R-loops can be immunoprecipitated using the S9.6 antibody, and the presence of R-loops assessed in specific gene loci prone to R-loop formation using quantitative PCR (DRIP-qPCR) (84,85). DRIP-qPCR was performed on the APOE gene locus in MDA-MB-436 BRCA1-mutant and WT-repleted breast cancer cells, a region known to form R-loops and the EGR-1 locus, which serves as a negative control as it does not form R-loops (Figure 5C, D). The negative control locus, EGR-1, had little R-loop formation in either BRCA1-deficient or WT-repleted cells (Figure 5C). As expected, we found that BRCA1-mutant cells have 2.2-fold more APOE locus R-loops than BRCA1 WT repleted cells. Consistent with the data above, DRIP-qPCR analysis demonstrated that TATDN2 depletion markedly increased R-loops at the APOE locus, but not at the EGR-1 locus. TATDN2 depletion increased R-loops by 3.3-fold in the BRCA1 WT cells and 6.9-fold in the BRCA1-mutant cells. RNase H1 treatment prior to qPCR analysis completely abolished the APOE R-loop signal, verifying that the assay measures R-loops (Figure 5D). It should be noted that while there is no statistical difference between the BRCA1-deficient and proficient daughter cells using the S9.6 confocal immunofluorescence assay, there is indeed a significant difference between those two types of cells in the DRIP-qPCR assay, which is more quantitative (Figure 5C, D). These *in vivo* data imply that cells with decreased

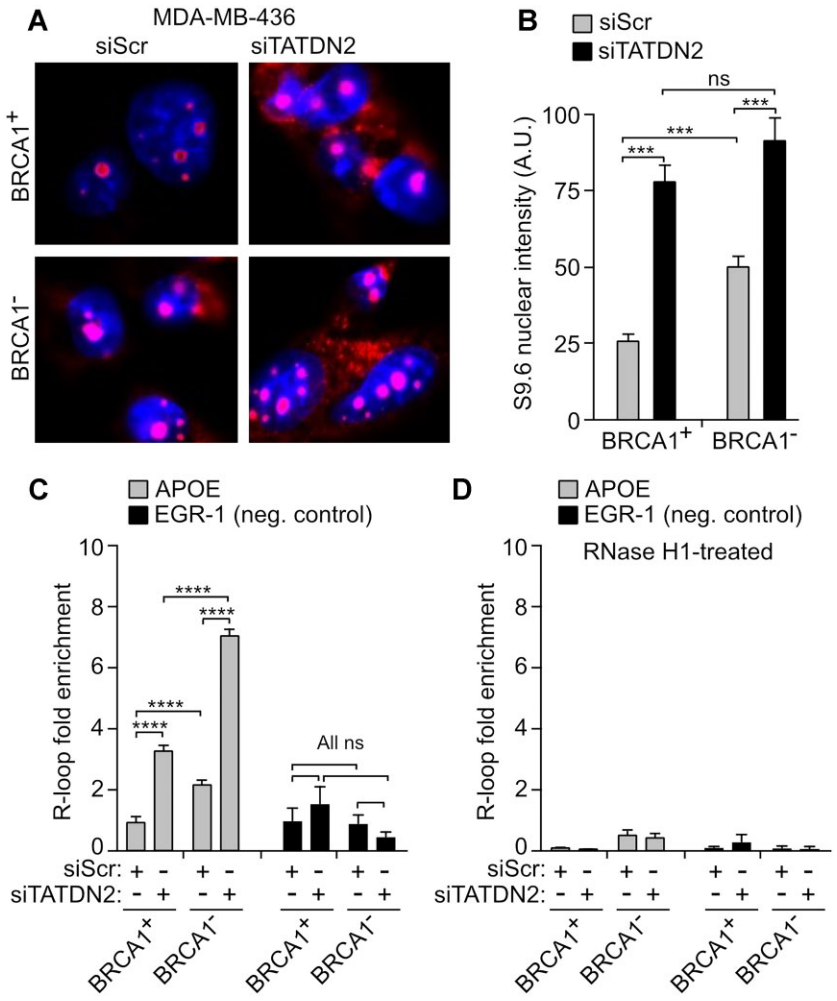

Figure 5. TATDN2 depletion increases R-loop formation *in vivo*. (**A**) Representative confocal immunofluorescent microscopic images of R-loops detected by S9.6 antibodies. (**B**) Quantitation of R-loop formation in MDA-MB-436 cells. Data expressed as a graphical representation of S9.6 confocal immunofluorescence intensity in BRCA1-deficient and WT repleted MDA-MB-436 cells with or without TATDN2 depletion; data are from >100 cells scanned per condition. The BRCA1-deficient cells showed increased R-loops without further stress when compared with the WT BRCA1 repleted cells. Statistically significant increases in R-loops are seen in both BRCA1-deficient and WT-repleted cells after TATDN2 depletion. (**C**) DRIP-qPCR analysis showing that depletion of TATDN2 increases R-loops at the APOE gene locus, and further increased by BRCA1-deficiency ($n = 3$). The EGR-1 locus does not form R-loops and serves as a negative control. (**D**) Loss of APOE signal after treatment with RNaseH1 demonstrates that these are indeed R-loops. There are no statistical differences between any of the data after RNaseH1 treatment.

R-loop resolution machinery are dependent on TATDN2 for resolution of these structures.

TATDN2 enhances replication fork progression when R-loops are excessive

Since R-loops can stall replication forks and complicate their repair, especially when they collide head on (17,44), we next tested whether huTATDN2 depletion would affect replication fork progression when R-loops are increased. We used ARV-825, a PROTAC inhibitor of BRD4 that increases R-loops and MDA-MB-436 cells, which are already stressed by increased R-loops due to lack of BRCA1 (53–56,82). We then treated the control and TATDN2-depleted cells with ARV-825 for 6 h, while at the same time labeling replication forks with CIdU. We then removed ARV-825 and labeled replication forks with IdU for 1 h to assess replication fork progression in response to R-loop stress (Figure 6A). We found that there was little difference in fork progression between control versus TATDN2-depleted cells without ARV-825 (Figure 6B, C). However, ARV-825 treatment of TATDN2-depleted cells resulted in markedly reduced replication fork progression in the presence of increased R-loops from ARV-825 (Figure 6B, C). In addition, TATDN2-depleted cells had shorter replication tracks even after release from ARV-825 (Figure 6D). These data suggest that increased R-loops in TATDN2-depleted cells slow replication fork progression even after the R-loop stressor was removed, implying that R-loop resolution in TATDN2-depleted cells is delayed compared to control cells. We also measured replication fork stalling and restart (73,74,76,77,80) in response to the replication stressor camptothecin in control and TATDN2-depleted, BRCA1-deficient MDA-MB-436 cells. We found that TATDN2 had no effect on replication fork stalling or restart when R-loops were not increased (Supplementary Figure S8).

TATDN2 promotes chromosomal stability and mitotic proficiency

Unresolved R-loops can lead to DSBs, most commonly from endonuclease nicking of the ssDNA in the R-loop, followed by collision with a replication fork (14–17). We therefore tested

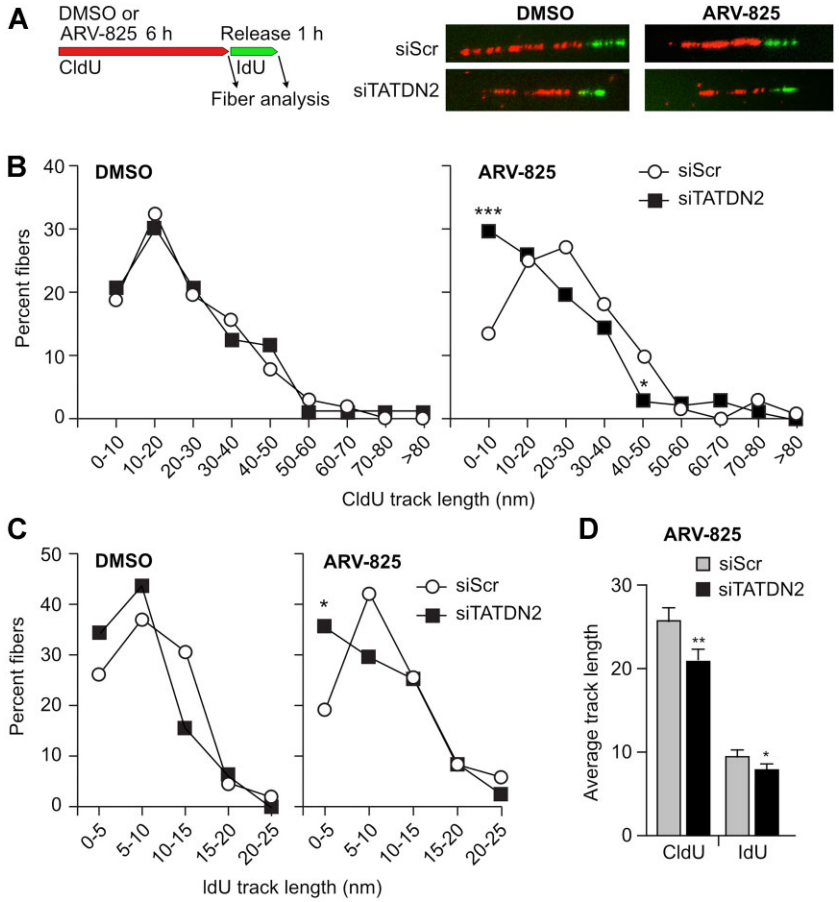

Figure 6. TATDN2 depletion suppresses replication fork progression when R-loops are increased in BRCA1-deficient MDA-MB-436 cells. (**A**) Schematic of the DNA fiber experiment and representative fiber images. R-loop formation was stimulated by ARV-825 over 6 h then removed. (**B**) CldU track lengths represent replication fork progression when ARV-825 is generating R-loops. (**C**) IdU track lengths represent replication fork progression after release from R-loop stress. TATDN2 depletion decreased replication fork progression both when ARV-825 is present and also after release from that R-loop stress. (**D**) Average replication track lengths in during (CldU) and after ARV-825 treatment (IdU). A total of 74–171 (average 118) fibers scored per condition.

whether TATDN2 depletion resulted in increased SS nicking of genomic DNA using an alkaline comet assay in MDA-MB-436 BRCA1-deficient cells. We found that TATDN2 depletion resulted in an increase in SS nicking as assessed by increased Comet tail moments (Figure 7A). If unrepaired, increased SS nicking at R-loops can lead to DSBs if not religated, as noted above (14–17). We used confocal immunofluorescence to detect γ-H2AX and BLM foci to measure DSB formation in untreated WT and TATDN2-depleted BRCA1 WT MCF7 breast cancer cells, which have much lower baseline DSBs than BRCA1-deficient cells (Figure 7B). We found that both γ-H2AX and BLM foci were markedly increased in the TATDN2 depleted cells, and that this was further increased by decatenation stress induced by the TOP2A inhibitor ICRF-193. We also found that TATDN2 depletion increased 53BP1 foci that co-localize with γ-H2AX foci in BRCA1 WT MCF7 cells (Supplementary Figure S9) (73,74,76,77,80,81), a further indication of increasing DSBs after TATDN2 depletion.

Unresolved R-loops can cause DSBs, which can result in free DS ends that can fuse with non-homologous ends of other broken chromosomes. Chromosomal fusion can cause defective chromosome segregation at mitosis, resulting in anaphase stalling, or if mitosis is completed, retained or shared chromosomes. We found that depletion of TATDN2 increased the fraction of mitotic cells in anaphase (Figure 7C). These data imply that TATDN2 is required for proper chromosome segregation in order to complete mitosis, common in cells with unreplicated regions or failed decatenation. Chromosome retention can be caused by centromere loss, seen as micronuclei. Shared chromosomes result when chromosome fusions result in gain of another centromere (dicentrics), and these are seen as chromosome bridges between daughter nuclei. One mechanism of such fusions is when DSBs at R-loops on disparate chromosomes aberrantly ligate (38–44). We found that TATDN2 depletion significantly increased both micronuclei and chromosome bridges in BRCA1-mutant MDA-MB-436 cells (Figure 7D), implying that TATDN2 may be important, least indirectly in preventing chromosomal fusions or unreplicated regions.

Discussion

In this study, we demonstrate that an IRE1-repressed miR, miR-4638-5p is synthetically lethal when reconstituted in BRCA1-deficient cells but far less so in a WT BRCA1-repleted derivative cell line (Figure 1). We tested whether miR-4638-5p could repress multiple other predicted target proteins and did not find any that were significantly repressed besides TATDN2 (Supplementary Figure S10), this study does not preclude other targets of miR4638-5p that are also important

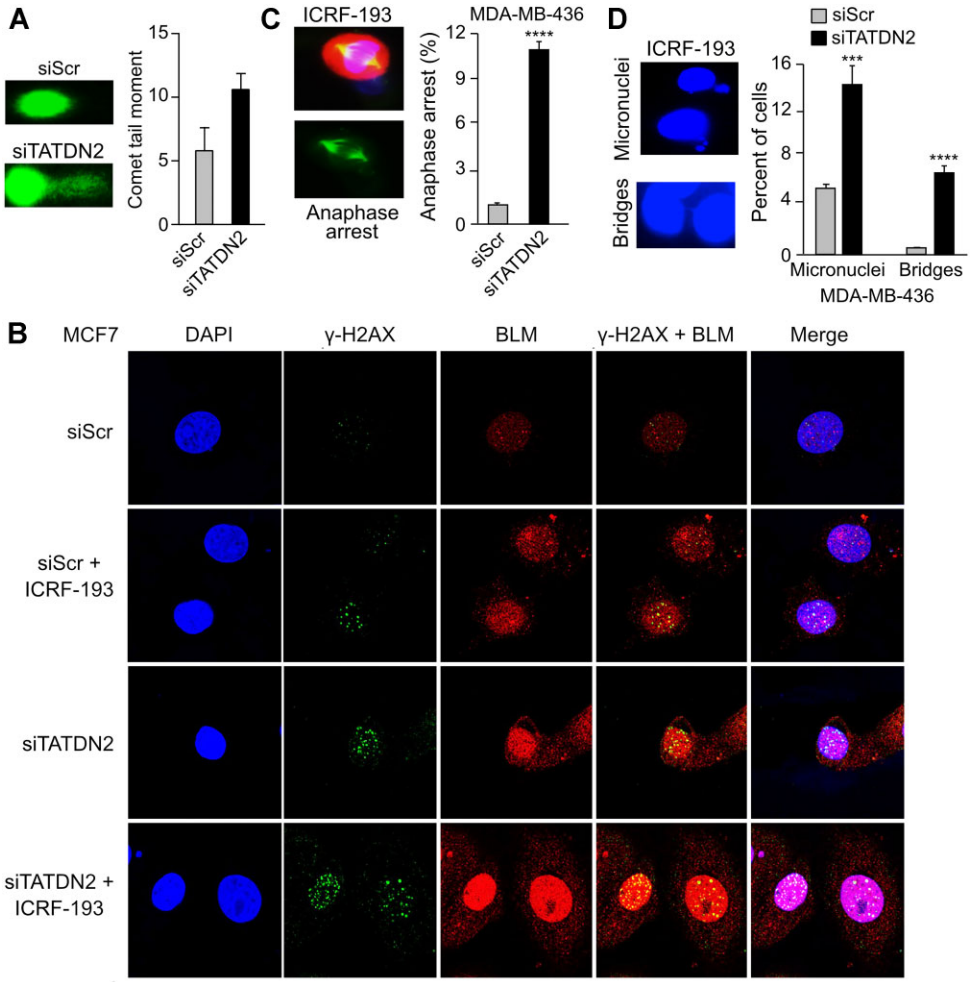

Figure 7. TATDN2 is required for genomic stability. (**A**) Alkaline Comet assays show increased genomic SS breaks in BRCA1-deficient MDA-MB-436 cells after depletion of TATDN2. (**B**) Depletion of TATDN2 alone or with chromosomal segregation stress induced by the decatenation inhibitor ICRF-193 results in increased γ-H2AX and BLM foci in BRCA1 WT MCF7 cells. (**C**) Depletion of TATDN2 alone or with ICRF-193 exposure increases anaphase arrest in BRCA1-deficient MDA-MB-436 breast cancer cells. (**D**) Depletion of TATDN2 increases chromosome segregation defects in BRCA1-deficient MDA-MB-436 cells, which results in retained chromosomes seen as micronuclei and shared chromosomes seen as nuclear bridges.

for BRCA1-deficient cell survival. Indeed, there may certainly be other relevant but undiscovered targets repressed by miR-4638-5p based on the fact that most miRs repress hundreds of mRNAs each. We also found that there are multiple other miRs affected by repression of IRE1 in BRCA1-deficient cells (Supplementary Figures S1, S10). It is likely that some of these may also generate lethality in BRCA1-deficient cells, like miR-4638-5p. Rather, this study presents extensive evidence that at least one mechanism for the synthetic lethality in BRCA1-deficient cells from miR4638-5p is via repression of TATDN2 protein expression (Figure 1).

TATDN2 is one of three human homologs of the TATD family whose canonical member is bacterial TatD, which is a 3′ SS DNA and RNA exonuclease (1–3). We characterized TATDN2 and found it is a 3′ RNA exonuclease and endonuclease that specifically degrades the RNA strand in R-loop triplexes (Figures 2, 4, S3, S4). Depleting TATDN2 leads to an increase in cellular R-loops, slowed replication and consequent genomic damage (Figures 5–7). One database of R-loop-associated proteins included TATDN2, consistent with the data presented here (88). TATDN2 also degrades DS RNA hairpin structures (Figure 2), implying that it could also play a role in the metabolism of miRs. While the maturation of miRs is well defined, the regulators of their half-life are not, and although beyond the scope of this study, it is tempting to speculate that TATDN2 also regulates degradation of mature or precursor miRs (66,67).

TATDN2 appears to have less activity than RnaseH1 in our *in vitro* assays (Figures 2 and 4), although it is difficult to correlate molar concentrations of TATDN2 with units of activity for RnaseH1. It should be noted that earlier characterizations of human RnaseH1 nuclease activities used up to 200 nM concentrations before convention dictated measuring it as units of activity (89–91). Those concentrations are higher than the TATDN2 concentrations used here (10–50 nM). The Kd for binding to RNA:DNA hybrid structures in the initial reports on human RnaseH1 was also higher than reported here for TATDN2 (90,91). It is possible that as isolation techniques for RNaseH1 improved, so did its activity, which may be the case here as well, since TATDN2 is difficult to purify and is labile after purification, so must be carefully stored. In addition, *in vitro* measurements of TATDN2 may not reflect its full activity *in vivo*, nor does possible lower relative activity necessarily mean that TATDN2 is not biologically relevant.

For most of the TATDN2 R-loop *in vitro* assays the majority of the substrate (∼80–90%, depending on the assay) was cleaved into smaller components, but just not digested down to the single nucleotide level as seen with RNaseH1, which may reflect TATDN2 RNA endonuclease activity as well, as such fragments could diffuse from the R-loop location, and thereby no longer be a substrate for TATDN2 since it is not hybridized to the DNA bubble. Since water was present in the reaction buffer, we assume that cleavage of the RNA in R-loops by TATDN2 generates a 5′-OH and 3′-P via hydrolysis of the phosphodiester bond, but this awaits further biochemical study.

There are several other RNases that are accepted to resolve R-loops besides RNaseH1, such as RNaseH2 (61), TREX1 (54,64) and XRN2 (48), so it should not be surprising that another alternative R-loop RNase exists. Most eukaryotic biological systems have redundancy. The sequence divergence of TATDN2 from the rest of the TATD family and the presence of these other R-loop RNases must have occurred under some specific selective pressure. It is likely that these different RNases function at distinct forms of R-loops or at distinct cell stages, such as seen with RNaseH2 compared to RNaseH1 (61).

The cyanobacteria species Synechocystis dtd3 gene product, which is closely related to human TATDN2 (25% identify in the nuclease domain) and bacterial TatD (35% indentity) was reported to hydrolyze D-aminoacyl-tRNAs (92). While it is possible that this could also be a function of TATDN2, there are two reasons why it may not be the case. First, TATDN2 has a unique long N-terminal region that mediates R-loop binding not seen in the dtd3 protein. Such a region could preferentially localize TATDN2 to R-loops, consistent with the finding that TATDN2 protein is found in the nucleus and not the cytoplasm. Second, dtd3 is more homologous to another bacterial protein, YcfH (40% identity), which has D-amino acyl-tRNA hydrolyzing activity, than to bacterial TatD which did not have that activity (92). However, it is recognized that increased incorporation of D-amino acids into proteins could cause unfolded protein stress, to which we reported that BRCA1-deficient cells are preferentially sensitive (71). Thus, loss of such an activity would indeed be synthetic lethal to BRCA1-deficient cancer cells such as seen here.

TATDN2 is a member of the large TATD family, which includes bacterial TatD (1,2). The tertiary structure of bacterial TatD and human TATDN1 and 3 have been reported (1,2,4), and the predicted structure of the C-terminal nuclease domain of human TATDN2 is available in the Alphafold-2 database. Bacterial TatD and human TATDN1 and 3 require the divalent cation Mg^{2+} for best catalytic activity, a feature shared with other DNase1 family nucleases (1–3). Using these structures, we predicted the amino acids that should chelate two potential divalent cations in human TATDN2: E593, E705 and D707. However, we found that only two of these residues, E593 and E705 were completely required for TATDN2 R-loop 3′ RNA exonuclease activity, while the D707A mutant TATDN2 still had some R-loop resolution activity (Figure 2). That only two acidic amino acids modeled for divalent cation chelation were needed for the R-loop RNase activity could imply that only one Mg^{2+} cation is absolutely required to be chelated by TATDN2 while the second cation maximizes activity. The catalytic site of TATDN2 also has two cysteines (C538 and C656) that are not present in other family members. Studies using non-denaturing gels in the absence of a divalent cation show that specific binding of TATDN2 to the R-loop structure requires the aforementioned long N-terminal disordered region unique to TATDN2 (Figure 3 and Supplementary Figure S3). It is possible that this unique N-terminal region could mediate binding to R-loops in specific regions or with specific structures that would provide the evolutionary pressure for its selection in addition to TATDN1 and 3. There are certainly R-loop structures that ubiquitous RNaseH1 does not metabolize (93–95). Such R-loop structures may have provided the selective pressure for further R-loop resolution enzymes like TATDN2. Expanding on this postulate, the evolutionary development of TATDN2 activity is consistent with the continued selective pressure of increasing R-loop formation with increased genome size and complexity of higher organisms.

Interestingly, TATDN2 can also relax catenated DNA by nicking it (Supplementary Figure S6). This is consistent with nicking of catenated DNA by zebrafish TATDN1 (12). The reason why this is consequential is that R-loop formation is a common, normal mechanism to relieve topological stress caused by negative supercoiling, such as from transcription or replication (33,34,96). Resolving an R-loop without resolving the underlying reason why it occurred does not solve the topological problem faced by the cell. It is possible that TATDN2 can perform both functions, resolving both the R-loop and the topological problem that led to its formation, by relaxing supercoiled DNA adjacent to the R-loop. The N-terminal region may be the switch between these activities, enhancing R-loop resolution and decreasing decatenation (Figure 3 and Supplementary Figure S6). Such a dual nuclease activity, resolving R-loops and nicking adjacent catenated DNA to relieve topological stress, would be as yet undescribed, and perhaps is the evolutionary pressure that promotes the differentiation of the TATD family.

Interestingly, BRCA1 can promote decatenation by enhancing TOP2A activity (97), providing another reason why TATDN2 would be important for BRCA1-deficient cell survival. The TATDN2 dual activity is likely essential for embryonic development, given that we found that TATDN2 homozygous knock-out mice die *in utero* before embryonic day 9.5 (Supplementary Figure S11). Consistent with this, mass spectroscopic analysis of proteins pulled down with immunoprecipitated Myc-tagged TATDN2 showed that the most common TATDN2-associated protein was TOP2A (Supplemental Table S1). Other common TATDN2-associated proteins were several nucleic acid binding zinc finger and RNA-binding proteins, including the RNA helicase DHX37 (Supplemental Table S1), attesting to a primary function of TATDN2 in RNA biology.

Pathologic R-loops cause genomic damage when encountered by replication forks or when the single DNA strand in an R-loop is nicked by any of several nucleases, including XPG and XPF, which function in nucleotide excision repair (98). We found that TATDN2 depletion significantly increased SS nicks in genomic DNA, consistent with SS DNA nicking of unresolved R-loops. When a replication fork collides with an R-loop with a SS nick, the nick is converted into a DSB which can be assessed by the presence of nuclear DSB foci. We discovered that TATDN2-depleted cells indeed had markedly increased γ-H2AX, BLM and 53BP1 nuclear foci, consistent with increased baseline DNA DSBs (Figure 7, Supplementary Figure S8). In normal cells, physiological R-loops predominate, and R-loop resolution is not as pressing as it is in cells

which lack one of the resolution components, as in BRCA1-mutant breast cancer cells. Thus, the discovery of increased R-loops, evidence of increased genomic DSBs (γ-H2AX and BLM foci) and decreased chromosomal segregation during mitosis in TATDN2-depleted BRCA1-mutant cancer cells is consistent with our finding that TATDN2 depletion is synthetically lethal in BRCA1-defective cells (Figure 1).

TATDN2 depletion did not appreciably alter the fraction of replication forks stalled by camptothecin, a classic inducer of replication stress, nor did it affect stalled fork repair and restart (Supplementary Figure S8). This is consistent with TATDN2 being a back-up pathway for R-loop resolution, most needed when R-loop concentrations become problematic. In this scenario, TATDN2 is not required for normal replication progression, but rather only when R-loops exceed what the cell's replication apparatus can tolerate. While TATDN2 depletion in WT BRCA1 cells increased genomic DSBs (Figure 7), such cells have better repair mechanisms to deal with DNA damage from unresolved R-loops (54–56).

However, loss of TATDN2 significantly decreased replication fork progression in BRCA1-deficient cells exposed to ARV-825 (Figure 6), an inducer of R-loops (82). TATDN2 depletion also decreased replication fork progression after release from ARV-825, implying that persistent R-loops continued to slow fork progression. The decrease in replication speed in either condition could be due to the presence of R-loops in front of stalled forks. While it is possible that TATDN2 plays a role in replication fork progression, TATDN2 depletion made little difference in fork progression before induction of increased R-loop formation (Figure 6). The impoverished replication progression after fork restart in TATDN2-depleted cells would lead to un-replicated regions that would not segregate properly during mitosis. Consistent with this, we observed anaphase arrest in BRCA1-defective cells with depleted TATDN2 (Figure 7C). This could be an alternative explanation for the failure to properly segregate chromosomes during mitosis in TATDN2-depleted cells besides either chromosomal fusion from unrepaired R-loop DSBs and failed chromosome decatenation. Thus, there are at least three potential mechanisms for the significant increase in shared chromosomes (bridging) and retained chromosomes (micronuclei) seen in the TATDN2-depleted BRCA1-deficient cells (Figure 7D), unreplicated regions persisting into mitosis, DSB fusions, or decreased decatenation.

The structural and functional characterization of TATDN1 and 3 nuclease domains were recently reported (4). This study found that TATDN1 and 3 had catalytic site structures similar to the previously reported bacterial TatD structure (1–3) and that each had DNA exonuclease and DNA abasic endonuclease function. We saw no appreciable DNA nuclease activity for TATDN2, except for minor abasic endonuclease activity at high concentrations and long autoradiogram exposures (Supplementary Figure S5). This nuclease activity of TATDN1 and 3 was present with multiple types of divalent cations, including Zn^{2+} and Ca^{2+} (4), which we did not find with TATDN2 (Supplementary Figure S3). TATDN1 and 3 structures both were found to chelate two divalent cations using three acidic amino acids. We found that TATDN2 required only two such acidic amino acids, E593 and E705, for full R-loop resolution activity. These were homologous to the cognate amino acids also required for TATDN1 and 3 nuclease activity (4). Human TATDN1 E112 interacts with two Zn^{2+} ions, and this residue corresponds to TATDN2 E593, while TATDN1 D222 coordinates one Zn^{2+} ion and corresponds to TATDN2 D707 (4). As mentioned, there are two cysteine residues in the catalytic domain of TATDN2 (Supplementary Figure S12) that are not present in the other family members, suggesting these could be targeted by a covalent inhibitor. It is possible that these differences in the catalytic domains of TATDN2 compared to the other human TATDN homologues mediate their distinct nuclease activities (Figures 2, 4 and Supplementary Figures S4–S6). Thus, there are at least three structural reasons for the unique activities of TATDN2, the long N-terminal domain, the two catalytic site cysteines and the lack of necessity of the third predicted chelator of the second divalent cation, D707.

PARP1/2 inhibitors represent a remarkable advance for the treatment of BRCA1-mutant cancers (99). There are currently four such inhibitors that are FDA-approved. However, almost all patients eventually relapse due to therapeutic resistance, and some patients cannot tolerate the gastrointestinal toxicity of these drugs (100). In addition, a small fraction of patients will develop myelodysplastic syndrome, a potentially fatal complication (101). Thus, additional drug targets are needed to treat these cancers, and TATDN2 may be a novel target for such intervention. While TATDN2 knock-out mice indicate that TATDN2 is crucial for embryonic development when both R-loop formation and replication are highly prevalent (Supplementary Figure S11), there may be less of a requirement for TATDN2 in normal adult cells, which have a lower replication rate and less risk from unresolved R-loops (Figure 1). The marked improvement in survival with TATDN2 depletion in WT BRCA1-repleted MDA-MB-436 cells demonstrate a potential therapeutic index between BRCA1-deficient tumors and normal tissues. Importantly, this study also identifies a potential anti-TATDN2 therapeutic agent, miR-4638-5p, potentially bypassing the requirement for a small molecule inhibitor. In conclusion, our findings demonstrate the TATDN2 axis as a novel target for treatment of BRCA1-mutant cancers and reveal potential approaches to exploit this axis for effective cancer treatment.

Data availability

The data underlying this article are available in MassIVE at https://massive.ucsd.edu/ProteoSAFe/static/massive.jsp and can be accessed under accession code MSV000092192. Materials are available upon request with a signed materials transfer agreement.

Supplementary data

Supplementary Data are available at NAR Online.

Acknowledgements

We thank the UT Southwestern Proteomics Core for assistance with mass spectrometry and the UTHSA Center for Innovative Drug Discovery and the Mays Cancer Center Drug Discovery and Structural Biology Shared Resource TATDN2 structure analysis and protein production and purification.

Author contributions: A.S.J., J.A.N. G.S. and R.H. designed, performed, analyzed experiments and wrote the manuscript. A.K., E.A.W., Y.Y., D.Z., D.T.S., M.S., M.X., Y.G., E.L., P.M., A.J.R.B. performed and analyzed experiments. A.P., S.O., D.Z. and P.S. designed experiments and provided critical input on the manuscript.

Funding

National Institutes of Health (NIH) [R01 CA139429]; Cancer Prevention and Research Institute of Texas [RP220269 to R.H.]; NIH [R35 CA241801 to P.S.]; American Lung Association [LCD-686552 to J.A.N.]; D.Z. and the Center for Innovative Drug Discovery and the Mays Cancer Center Drug Discovery and Structural Biology Shared Resource are supported by CPRIT Core Facility Award [RP210208]; NIH-NCI [P30 CA054174]; Y.G. was supported by NIH [R01AI161363]; Welch Foundation [AQ-2101]; A.B. was supported by NIH [1R01CA241554]; CPRIT [RP150445 and SU2C-CRUK RT6187]. Funding for open access charge: University of Texas Health Science Center San Antonio.

Conflict of interest statement

None declared.

References

1. Lee,K.Y., Cheon,S.H., Kim,D.G., Lee,S.J. and Lee,B.J. (2020) A structural study of TatD from *Staphylococcus aureus* elucidates a putative DNA-binding mode of a Mg^{2+}-dependent nuclease. *IUCrJ*, **7**, 509–521.
2. Chen,Y.C., Li,C.L., Hsiao,Y.Y., Duh,Y. and Yuan,H.S. (2014) Structure and function of TatD exonuclease in DNA repair. *Nucleic Acids Res.*, **42**, 10776–10785.
3. Singh,D., Rahi,A., Kumari,R., Gupta,V., Gautam,G., Aggarwal,S., Rehan,M. and Bhatnagar,R. (2019) Computational and mutational analysis of TatD DNase of *Bacillus anthracis*. *J. Cell. Biochem.*, **120**, 11318–11330.
4. Dorival,J. and Eichman,B.F. (2023) Human and bacterial TatD enzymes exhibit apurinic/apyrimidinic (AP) endonuclease activity. *Nucleic Acids Res.*, **51**, 2838–2849.
5. Piovesan,D., Monzon,A.M. and Tosatto,S.C.E. (2022) Intrinsic protein disorder and conditional folding in AlphaFoldDB. *Protein Sci.*, **31**, e4466.
6. Skolnick,J., Gao,M., Zhou,H. and Singh,S. (2021) AlphaFold 2: why it works and its implications for understanding the relationships of protein sequence, structure, and function. *J. Chem. Inf. Model.*, **61**, 4827–4831.
7. Jumper,J., Evans,R., Pritzel,A., Green,T., Figurnov,M., Ronneberger,O., Tunyasuvunakool,K., Bates,R., Zidek,A., Potapenko,A., *et al.* (2021) Highly accurate protein structure prediction with AlphaFold. *Nature*, **596**, 583–589.
8. Qiu,J., Yoon,J.H. and Shen,B. (2005) Search for apoptotic nucleases in yeast: role of Tat-D nuclease in apoptotic DNA degradation. *J. Biol. Chem.*, **280**, 15370–15379.
9. Gannavaram,S. and Debrabant,A. (2012) Involvement of TatD nuclease during programmed cell death in the protozoan parasite *Trypanosoma brucei*. *Mol. Microbiol.*, **83**, 926–935.
10. Zhang,Z., Liang,Y., Yu,L., Chen,M., Guo,Y., Kang,Z., Qu,C., Tian,C., Zhang,D. and Liu,M. (2021) TatD DNases contribute to biofilm formation and virulence in *Trueperella pyogenes*. *Front. Microbiol.*, **12**, 758465.
11. Chang,Z., Jiang,N., Zhang,Y., Lu,H., Yin,J., Wahlgren,M., Cheng,X., Cao,Y. and Chen,Q. (2016) The TatD-like DNase of plasmodium is a virulence factor and a potential malaria vaccine candidate. *Nat. Commun.*, **7**, 11537.
12. Yang,H., Liu,C., Jamsen,J., Wu,Z., Wang,Y., Chen,J., Zheng,L. and Shen,B. (2012) The DNase domain-containing protein TATDN1 plays an important role in chromosomal segregation and cell cycle progression during zebrafish eye development. *Cell Cycle*, **11**, 4626–4632.
13. Thomas,M., White,R.L. and Davis,R.W. (1976) Hybridization of RNA to double-stranded DNA: formation of R-loops. *Proc. Natl. Acad. Sci. U.S.A.*, **73**, 2294–2298.
14. Niehrs,C. and Luke,B. (2020) Regulatory R-loops as facilitators of gene expression and genome stability. *Nat. Rev. Mol. Cell Biol.*, **21**, 167–178.
15. Mackay,R.P., Xu,Q. and Weinberger,P.M. (2020) R-loop physiology and pathology: a brief review. *DNA Cell Biol.*, **39**, 1914–1925.
16. Rinaldi,C., Pizzul,P., Longhese,M.P. and Bonetti,D. (2020) Sensing R-loop-associated DNA damage to safeguard genome stability. *Front. Cell Dev. Biol.*, **8**, 618157.
17. Brickner,J.R., Garzon,J.L. and Cimprich,K.A. (2022) Walking a tightrope: the complex balancing act of R-loops in genome stability. *Mol. Cell*, **82**, 2267–2297.
18. Holt,I.J. (2022) R-loops and mitochondrial DNA metabolism. *Methods Mol. Biol.*, **2528**, 173–202.
19. Posse,V., Al-Behadili,A., Uhler,J.P., Clausen,A.R., Reyes,A., Zeviani,M., Falkenberg,M. and Gustafsson,C.M. (2019) RNase H1 directs origin-specific initiation of DNA replication in human mitochondria. *PLoS Genet.*, **15**, e1007781.
20. Tian,M. and Alt,F.W. (2000) Transcription-induced cleavage of immunoglobulin switch regions by nucleotide excision repair nucleases in vitro. *J. Biol. Chem.*, **275**, 24163–24172.
21. So,C.C. and Martin,A. (2019) DSB structure impacts DNA recombination leading to class switching and chromosomal translocations in human B cells. *PLoS Genet.*, **15**, e1008101.
22. Teng,Y., Yadav,T., Duan,M., Tan,J., Xiang,Y., Gao,B., Xu,J., Liang,Z., Liu,Y., Nakajima,S., *et al.* (2018) ROS-induced R loops trigger a transcription-coupled but BRCA1/2-independent homologous recombination pathway through CSB. *Nat. Commun.*, **9**, 4115.
23. Yasuhara,T., Kato,R., Hagiwara,Y., Shiotani,B., Yamauchi,M., Nakada,S., Shibata,A. and Miyagawa,K. (2018) Human Rad52 promotes XPG-mediated R-loop processing to initiate transcription-associated homologous recombination repair. *Cell*, **175**, 558–570.
24. Chen,P.B., Chen,H.V., Acharya,D., Rando,O.J. and Fazzio,T.G. (2015) R loops regulate promoter-proximal chromatin architecture and cellular differentiation. *Nat. Struct. Mol. Biol.*, **22**, 999–1007.
25. Ginno,P.A., Lott,P.L., Christensen,H.C., Korf,I. and Chedin,F. (2012) R-loop formation is a distinctive characteristic of unmethylated human CpG island promoters. *Mol. Cell*, **45**, 814–825.
26. Ginno,P.A., Lim,Y.W., Lott,P.L., Korf,I. and Chedin,F. (2013) GC skew at the 5' and 3' ends of human genes links R-loop formation to epigenetic regulation and transcription termination. *Genome Res.*, **23**, 1590–1600.
27. Castellano-Pozo,M., Santos-Pereira,J.M., Rondon,A.G., Barroso,S., Andujar,E., Perez-Alegre,M., Garcia-Muse,T. and Aguilera,A. (2013) R loops are linked to histone H3 S10 phosphorylation and chromatin condensation. *Mol. Cell*, **52**, 583–590.
28. Zhou,H., Li,L., Wang,Q., Hu,Y., Zhao,W., Gautam,M. and Li,L. (2020) H3K9 demethylation-induced R-loop accumulation is linked to disorganized nucleoli. *Front. Genet.*, **11**, 43.
29. Fazzio,T.G. (2016) Regulation of chromatin structure and cell fate by R-loops. *Transcription*, **7**, 121–126.
30. Chedin,F. (2016) Nascent connections: r-loops and chromatin patterning. *Trends Genet.*, **32**, 828–838.
31. Drolet,M., Bi,X. and Liu,L.F. (1994) Hypernegative supercoiling of the DNA template during transcription elongation in vitro. *J. Biol. Chem.*, **269**, 2068–2074.
32. Drolet,M. (2006) Growth inhibition mediated by excess negative supercoiling: the interplay between transcription elongation, R-loop formation and DNA topology. *Mol. Microbiol.*, **59**, 723–730.
33. Stolz,R., Sulthana,S., Hartono,S.R., Malig,M., Benham,C.J. and Chedin,F. (2019) Interplay between DNA sequence and negative superhelicity drives R-loop structures. *Proc. Natl. Acad. Sci. USA*, **116**, 6260–6269.

34. Phoenix,P., Raymond,M.A., Masse,E. and Drolet,M. (1997) Roles of DNA topoisomerases in the regulation of R-loop formation in vitro. *J. Biol. Chem.*, **272**, 1473–1479.
35. El Hage,A., French,S.L., Beyer,A.L. and Tollervey,D. (2010) Loss of topoisomerase I leads to R-loop-mediated transcriptional blocks during ribosomal RNA synthesis. *Genes Dev.*, **24**, 1546–1558.
36. Manzo,S.G., Hartono,S.R., Sanz,L.A., Marinello,J., De Biasi,S., Cossarizza,A., Capranico,G. and Chedin,F. (2018) DNA topoisomerase I differentially modulates R-loops across the human genome. *Genome Biol.*, **19**, 100.
37. Masse,E. and Drolet,M. (1999) *Escherichia coli* DNA topoisomerase I inhibits R-loop formation by relaxing transcription-induced negative supercoiling. *J. Biol. Chem.*, **274**, 16659–16664.
38. Wahba,L., Gore,S.K. and Koshland,D. (2013) The homologous recombination machinery modulates the formation of RNA–DNA hybrids and associated chromosome instability. *Elife*, **2**, e00505.
39. Skourti-Stathaki,K. and Proudfoot,N.J. (2014) A double-edged sword: r loops as threats to genome integrity and powerful regulators of gene expression. *Genes Dev.*, **28**, 1384–1396.
40. Wimberly,H., Shee,C., Thornton,P.C., Sivaramakrishnan,P., Rosenberg,S.M. and Hastings,P.J. (2013) R-loops and nicks initiate DNA breakage and genome instability in non-growing Escherichia coli. *Nat. Commun.*, **4**, 2115.
41. Gan,W., Guan,Z., Liu,J., Gui,T., Shen,K., Manley,J.L. and Li,X. (2011) R-loop-mediated genomic instability is caused by impairment of replication fork progression. *Genes Dev.*, **25**, 2041–2056.
42. Helmrich,A., Ballarino,M. and Tora,L. (2011) Collisions between replication and transcription complexes cause common fragile site instability at the longest human genes. *Mol. Cell*, **44**, 966–977.
43. Lang,K.S., Hall,A.N., Merrikh,C.N., Ragheb,M., Tabakh,H., Pollock,A.J., Woodward,J.J., Dreifus,J.E. and Merrikh,H. (2017) Replication-transcription conflicts generate R-loops that orchestrate bacterial stress survival and pathogenesis. *Cell*, **170**, 787–799.
44. Hamperl,S., Bocek,M.J., Saldivar,J.C., Swigut,T. and Cimprich,K.A. (2017) Transcription-replication conflict orientation modulates R-loop levels and activates distinct DNA damage responses. *Cell*, **170**, 774–786.
45. Roy,D., Zhang,Z., Lu,Z., Hsieh,C.L. and Lieber,M.R. (2010) Competition between the RNA transcript and the nontemplate DNA strand during R-loop formation in vitro: a nick can serve as a strong R-loop initiation site. *Mol. Cell. Biol.*, **30**, 146–159.
46. Moreira,M.C., Klur,S., Watanabe,M., Nemeth,A.H., Le Ber,I., Moniz,J.C., Tranchant,C., Aubourg,P., Tazir,M., Schols,L., *et al.* (2004) Senataxin, the ortholog of a yeast RNA helicase, is mutant in ataxia-ocular apraxia 2. *Nat. Genet.*, **36**, 225–227.
47. Cohen,S., Puget,N., Lin,Y.L., Clouaire,T., Aguirrebengoa,M., Rocher,V., Pasero,P., Canitrot,Y. and Legube,G. (2018) Senataxin resolves RNA:DNA hybrids forming at DNA double-strand breaks to prevent translocations. *Nat. Commun.*, **9**, 533.
48. Skourti-Stathaki,K., Proudfoot,N.J. and Gromak,N. (2011) Human senataxin resolves RNA/DNA hybrids formed at transcriptional pause sites to promote Xrn2-dependent termination. *Mol. Cell*, **42**, 794–805.
49. Pan,X., Chen,Y., Biju,B., Ahmed,N., Kong,J., Goldenberg,M., Huang,J., Mohan,N., Klosek,S., Parsa,K., *et al.* (2019) FANCM suppresses DNA replication stress at ALT telomeres by disrupting TERRA R-loops. *Sci. Rep.*, **9**, 19110.
50. Garcia-Rubio,M.L., Perez-Calero,C., Barroso,S.I., Tumini,E., Herrera-Moyano,E., Rosado,I.V. and Aguilera,A. (2015) The Fanconi anemia pathway protects genome integrity from R-loops. *PLoS Genet.*, **11**, e1005674.
51. Okamoto,Y., Abe,M., Itaya,A., Tomida,J., Ishiai,M., Takaori-Kondo,A., Taoka,M., Isobe,T. and Takata,M. (2019) FANCD2 protects genome stability by recruiting RNA processing enzymes to resolve R-loops during mild replication stress. *FEBS J.*, **286**, 139–150.
52. Schwab,R.A., Nieminuszczy,J., Shah,F., Langton,J., Lopez Martinez,D., Liang,C.C., Cohn,M.A., Gibbons,R.J., Deans,A.J. and Niedzwiedz,W. (2015) The Fanconi anemia pathway maintains genome stability by coordinating replication and transcription. *Mol. Cell*, **60**, 351–361.
53. San Martin Alonso,M. and Noordermeer,S.M. (2021) Untangling the crosstalk between BRCA1 and R-loops during DNA repair. *Nucleic Acids Res.*, **49**, 4848–4863.
54. Bhatia,V., Barroso,S.I., Garcia-Rubio,M.L., Tumini,E., Herrera-Moyano,E. and Aguilera,A. (2014) BRCA2 prevents R-loop accumulation and associates with TREX-2 mRNA export factor PCID2. *Nature*, **511**, 362–365.
55. Wang,Y., Ma,B., Liu,X., Gao,G., Che,Z., Fan,M., Meng,S., Zhao,X., Sugimura,R., Cao,H., *et al.* (2022) ZFP281-BRCA2 prevents R-loop accumulation during DNA replication. *Nat. Commun.*, **13**, 3493.
56. Hatchi,E., Skourti-Stathaki,K., Ventz,S., Pinello,L., Yen,A., Kamieniarz-Gdula,K., Dimitrov,S., Pathania,S., McKinney,K.M., Eaton,M.L., *et al.* (2015) BRCA1 recruitment to transcriptional pause sites is required for R-loop-driven DNA damage repair. *Mol. Cell*, **57**, 636–647.
57. Tran,P.L.T., Pohl,T.J., Chen,C.F., Chan,A., Pott,S. and Zakian,V.A. (2017) PIF1 family DNA helicases suppress R-loop mediated genome instability at tRNA genes. *Nat. Commun.*, **8**, 15025.
58. Cristini,A., Groh,M., Kristiansen,M.S. and Gromak,N. (2018) RNA/DNA hybrid interactome identifies DXH9 as a molecular player in transcriptional termination and R-loop-associated DNA damage. *Cell Rep.*, **23**, 1891–1905.
59. Yuan,W., Al-Hadid,Q., Wang,Z., Shen,L., Cho,H., Wu,X. and Yang,Y. (2021) TDRD3 promotes DHX9 chromatin recruitment and R-loop resolution. *Nucleic Acids Res.*, **49**, 8573–8591.
60. Lima,W.F., Murray,H.M., Damle,S.S., Hart,C.E., Hung,G., De Hoyos,C.L., Liang,X.H. and Crooke,S.T. (2016) Viable RNaseH1 knockout mice show RNaseH1 is essential for R loop processing, mitochondrial and liver function. *Nucleic Acids Res.*, **44**, 5299–5312.
61. Lockhart,A., Pires,V.B., Bento,F., Kellner,V., Luke-Glaser,S., Yakoub,G., Ulrich,H.D. and Luke,B. (2019) RNase H1 and H2 are differentially regulated to process RNA–DNA hybrids. *Cell Rep.*, **29**, 2890–2900.
62. Cristini,A., Tellier,M., Constantinescu,F., Accalai,C., Albulescu,L.O., Heiringhoff,R., Bery,N., Sordet,O., Murphy,S. and Gromak,N. (2022) RNase H2, mutated in Aicardi-Goutieres syndrome, resolves co-transcriptional R-loops to prevent DNA breaks and inflammation. *Nat. Commun.*, **13**, 2961.
63. Nguyen,H.D., Yadav,T., Giri,S., Saez,B., Graubert,T.A. and Zou,L. (2017) Functions of replication protein A as a sensor of R loops and a regulator of RNaseH1. *Mol. Cell*, **65**, 832–847.
64. Dominguez-Sanchez,M.S., Barroso,S., Gomez-Gonzalez,B., Luna,R. and Aguilera,A. (2011) Genome instability and transcription elongation impairment in human cells depleted of THO/TREX. *PLos Genet.*, **7**, e1002386.
65. Luna,R., Rondon,A.G., Perez-Calero,C., Salas-Armenteros,I. and Aguilera,A. (2019) The THO complex as a paradigm for the prevention of cotranscriptional R-loops. *Cold Spring Harb. Symp. Quant. Biol.*, **84**, 105–114.
66. Dexheimer,P.J. and Cochella,L. (2020) MicroRNAs: from mechanism to organism. *Front. Cell Dev. Biol.*, **8**, 409.
67. Treiber,T., Treiber,N. and Meister,G. (2019) Regulation of microRNA biogenesis and its crosstalk with other cellular pathways. *Nat. Rev. Mol. Cell Biol.*, **20**, 5–20.
68. Gonzalo,L., Tossolini,I., Gulanicz,T., Cambiagno,D.A., Kasprowicz-Maluski,A., Smolinski,D.J., Mammarella,M.F., Ariel,F.D., Marquardt,S., Szweykowska-Kulinska,Z., *et al.* (2022) R-loops at microRNA encoding loci promote co-transcriptional processing of pri-miRNAs in plants. *Nat. Plants*, **8**, 402–418.

69. Li,Y., Tong,Y., Liu,J. and Lou,J. (2022) The role of microRNA in DNA damage response. *Front. Genet.*, **13**, 850038.
70. Peraza-Vega,R.I., Valverde,M. and Rojas,E. (2022) Interactions between miRNAs and double-strand breaks DNA repair genes, pursuing a fine-tuning of repair. *Int. J. Mol. Sci.*, **23**, 3231–3248.
71. Hromas,R., Srinivasan,G., Yang,M., Jaiswal,A., Totterdale,T.A., Phillips,L., Kirby,A., Khodayari,N., Brantley,M., Williamson,E.A., *et al.* (2022) BRCA1 mediates protein homeostasis through the ubiquitination of PERK and IRE1. *Iscience*, **25**, 105626.
72. Zhang,K., Liu,H., Song,Z., Jiang,Y., Kim,H., Samavati,L., Nguyen,H.M. and Yang,Z.Q. (2020) The UPR transducer IRE1 promotes breast cancer malignancy by degrading tumor suppressor microRNAs. *Iscience*, **23**, 101503.
73. Hromas,R., Kim,H.S., Sidhu,G., Williamson,E.A., Jaiswal,A., Totterdale,T.A., Nole,J., Lee,S.-H., Nickoloff,J.A. and Kong,K.Y. (2017) The endonuclease EEPD1 mediates synthetic lethality in RAD52-depleted BRCA1-mutant breast cancer cells. *Breast Cancer Res.*, **19**, 122.
74. Wu,Y., Lee,S.H., Williamson,E.A., Reinert,B.L., Cho,J.H., Xia,F., Jaiswal,A.S., Srinivasan,G., Patel,B., Brantley,A., *et al.* (2015) EEPD1 rescues stressed replication forks and maintains genome stability by promoting end resection and homologous recombination repair. *PLoS Genet.*, **11**, e1005675.
75. Jaiswal,A.S., Williamson,E.A., Srinivasan,G., Kong,K., Lomelino,C.L., McKenna,R., Walter,C., Sung,P., Narayan,S. and Hromas,R. (2020) The splicing component ISY1 regulates APE1 in base excision repair. *DNA Repair (Amst.)*, **86**, 102769.
76. Jaiswal,A.S., Kim,H.S., Scharer,O.D., Sharma,N., Williamson,E.A., Srinivasan,G., Phillips,L., Kong,K., Arya,S., Misra,A., *et al.* (2023) EEPD1 promotes repair of oxidatively-stressed replication forks. *NAR Cancer*, **5**, zcac044.
77. Srinivasan,G., Williamson,E.A., Kong,K., Jaiswal,A.S., Huang,G., Kim,H.S., Scharer,O., Zhao,W., Burma,S., Sung,P., *et al.* (2019) MiR223-3p promotes synthetic lethality in BRCA1-deficient cancers. *Proc. Natl. Acad. Sci. U.S.A.*, **116**, 17438–17443.
78. Hromas,R., Williamson,E., Fnu,S., Lee,Y.-J., Park,S.-J., Beck,B.D., You,J.-S., Laitao,A., Nickoloff,J.A. and Lee,S.-H. (2012) Chk1 phosphorylation of Metnase enhances DNA repair but inhibits replication fork restart. *Oncogene*, **31**, 4245–4254.
79. Jaiswal,A.S., Panda,H., Law,B.K., Sharma,J., Jani,J., Hromas,R. and Narayan,S. (2015) NSC666715 and its analogs inhibit strand-displacement activity of DNA polymerase β and potentiate temozolomide-induced DNA damage, senescence and apoptosis in colorectal cancer cells. *PLoS One*, **10**, e0123808.
80. Kim,H.S., Nickoloff,J.A., Wu,Y., Williamson,E.A., Sidhu,G.S., Reinert,B.L., Jaiswal,A.S., Srinivasan,G., Patel,B., Kong,K., *et al.* (2017) Endonuclease EEPD1 is a gatekeeper for repair of stressed replication forks. *J. Biol. Chem.*, **292**, 2795–2804.
81. Wray,J., Williamson,E.A., Fnu,S., Lee,S.-H., Libby,E., Willman,C.L., Nickoloff,J.A. and Hromas,R. (2009) Metnase mediates chromosome decatenation in acute leukemia cells. *Blood*, **114**, 1852–1858.
82. Lam,F.C., Kong,Y.W., Huang,Q., Vu Han,T.L., Maffa,A.D., Kasper,E.M. and Yaffe,M.B. (2020) BRD4 prevents the accumulation of R-loops and protects against transcription-replication collision events and DNA damage. *Nat. Commun.*, **11**, 4083.
83. Dutta,A., Kwon,Y. and Sung,P. (2022) Biochemical analysis of RNA–DNA hybrid and R-loop unwinding via motor proteins. *Methods Mol. Biol.*, **2528**, 305–316.
84. Sanz,L.A. and Chedin,F. (2019) High-resolution, strand-specific R-loop mapping via S9.6-based DNA-RNA immunoprecipitation and high-throughput sequencing. *Nat. Protoc.*, **14**, 1734–1755.
85. Garcia-Rubio,M., Barroso,S.I. and Aguilera,A. (2018) Detection of DNA-RNA hybrids in vivo. *Methods Mol. Biol.*, **1672**, 347–361.
86. Salas-Armenteros,I., Perez-Calero,C., Bayona-Feliu,A., Tumini,E., Luna,R. and Aguilera,A. (2017) Human THO-Sin3A interaction reveals new mechanisms to prevent R-loops that cause genome instability. *EMBO J.*, **36**, 3532–3547.
87. Chen,D., Shan,J., Zhu,W.G., Qin,J. and Gu,W. (2010) Transcription-independent ARF regulation in oncogenic stress-mediated p53 responses. *Nature*, **464**, 624–627.
88. Yan,Q., Wulfridge,P., Doherty,J., Fernandez-Luna,J.L., Real,P.J., Tang,H.Y. and Sarma,K. (2022) Proximity labeling identifies a repertoire of site-specific R-loop modulators. *Nat. Commun.*, **13**, 53–59.
89. Gaidamakov,S.A., Gorshkova,I.I., Schuck,P., Steinbach,P.J., Yamada,H., Crouch,R.J. and Cerritelli,S.M. (2005) Eukaryotic RNases H1 act processively by interactions through the duplex RNA-binding domain. *Nucleic Acids Res.*, **33**, 2166–2175.
90. Wu,H., Lima,W.F. and Crooke,S.T. (1999) Properties of cloned and expressed human RNase H1. *J. Biol. Chem.*, **274**, 28270–28278.
91. Wu,H., Lima,W.F. and Crooke,S.T. (2001) Investigating the structure of human RNase H1 by site-directed mutagenesis. *J. Biol. Chem.*, **276**, 23547–23553.
92. Wydau,S., van der Rest,G., Aubard,C., Plateau,P. and Blanquet,S. (2009) Widespread distribution of cell defense against D-aminoacyl-tRNAs. *J. Biol. Chem.*, **284**, 14096–14104.
93. Lima,W.F., Rose,J.B., Nichols,J.G., Wu,H., Migawa,M.T., Wyrzykiewicz,T.K., Vasquez,G., Swayze,E.E. and Crooke,S.T. (2007) The positional influence of the helical geometry of the heteroduplex substrate on human RNase H1 catalysis. *Mol. Pharmacol.*, **71**, 73–82.
94. Lima,W.F., Rose,J.B., Nichols,J.G., Wu,H., Migawa,M.T., Wyrzykiewicz,T.K., Siwkowski,A.M. and Crooke,S.T. (2007) Human RNase H1 discriminates between subtle variations in the structure of the heteroduplex substrate. *Mol. Pharmacol.*, **71**, 83–91.
95. Lima,W.F. and Crooke,S.T. (1997) Binding affinity and specificity of Escherichia coli RNase H1: impact on the kinetics of catalysis of antisense oligonucleotide-RNA hybrids. *Biochemistry*, **36**, 390–398.
96. Chedin,F. and Benham,C.J. (2020) Emerging roles for R-loop structures in the management of topological stress. *J. Biol. Chem.*, **295**, 4684–4695.
97. Lou,Z., Minter-Dykhouse,K. and Chen,J. (2005) BRCA1 participates in DNA decatenation. *Nat. Struct. Mol. Biol.*, **12**, 589–593.
98. Goulielmaki,E., Tsekrekou,M., Batsiotos,N., Ascensao-Ferreira,M., Ledaki,E., Stratigi,K., Chatzinikolaou,G., Topalis,P., Kosteas,T., Altmuller,J., *et al.* (2021) The splicing factor XAB2 interacts with ERCC1-XPF and XPG for R-loop processing. *Nat. Commun.*, **12**, 3153.
99. Cortesi,L., Rugo,H.S. and Jackisch,C. (2021) An overview of PARP inhibitors for the treatment of breast cancer. *Target. Oncol.*, **16**, 255–282.
100. Liu,Y., Meng,J. and Wang,G. (2018) Risk of selected gastrointestinal toxicities associated with poly (ADP-ribose) polymerase (PARP) inhibitors in the treatment of ovarian cancer: a meta-analysis of published trials. *Drug Des. Devel. Ther.*, **12**, 3013–3019.
101. Morice,P.M., Leary,A., Dolladille,C., Chretien,B., Poulain,L., Gonzalez-Martin,A., Moore,K., O'Reilly,E.M., Ray-Coquard,I. and Alexandre,J. (2021) Myelodysplastic syndrome and acute myeloid leukaemia in patients treated with PARP inhibitors: a safety meta-analysis of randomised controlled trials and a retrospective study of the WHO pharmacovigilance database. *Lancet Haematol.*, **8**, e122–e134.

Received: May 28, 2023. **Revised:** October 3, 2023. **Editorial Decision:** October 8, 2023. **Accepted:** October 18, 2023